Systematic KMTNet Planetary Anomaly Search. IX. Complete Sample of 2016 Prime-field Planets

In-Gu Shin[1], Jennifer C. Yee[1], Weicheng Zang[1,2], Hongjing Yang[2], Kyu-Ha Hwang[3], Cheongho Han[4],
Andrew Gould[5,6], Andrzej Udalski[7], Ian A. Bond[8]
(Leading authors),
Michael D. Albrow[9], Sun-Ju Chung[3], Youn Kil Jung[3,10], Yoon-Hyun Ryu[3], Yossi Shvartzvald[11], Sang-Mok Cha[3,12],
Dong-Jin Kim[3], Seung-Lee Kim[3], Chung-Uk Lee[3], Dong-Joo Lee[3], Yongseok Lee[3,12], Byeong-Gon Park[3],
Richard W. Pogge[6]
(The KMTNet Collaboration),
Przemek Mróz[7], Michał K. Szymański[7], Jan Skowron[7], Radosław Poleski[7], Igor Soszyński[7], Paweł Pietrukowicz[7],
Szymon Kozłowski[7], Krzysztof A. Rybicki[7,11], Patryk Iwanek[7], Krzysztof Ulaczyk[13], Marcin Wrona[7],
Mariusz Gromadzki[7]
(The OGLE Collaboration),
and
Fumio Abe[14], Richard Barry[15], David P. Bennett[15,16], Aparna Bhattacharya[15,16], Hirosane Fujii[14], Akihiko Fukui[17,18],
Ryusei Hamada[19], Yuki Hirao[19], Stela Ishitani Silva[15,20], Yoshitaka Itow[14], Rintaro Kirikawa[19], Iona Kondo[19],
Naoki Koshimoto[21], Yutaka Matsubara[14], Shota Miyazaki[19], Yasushi Muraki[14], Greg Olmschenk[15], Clément Ranc[22],
Nicholas J. Rattenbury[23], Yuki Satoh[19], Takahiro Sumi[19], Daisuke Suzuki[19], Mio Tomoyoshi[19], Paul J. Tristram[24],
Aikaterini Vandorou[15,16], Hibiki Yama[19], and Kansuke Yamashita[19]
(the MOA Collaboration)

[1] Center for Astrophysics | Harvard & Smithsonian, 60 Garden Street, Cambridge, MA 02138, USA; ingushin@gmail.com
[2] Department of Astronomy, Tsinghua University, Beijing 100084, People's Republic of China
[3] Korea Astronomy and Space Science Institute, Daejon 34055, Republic of Korea
[4] Department of Physics, Chungbuk National University, Cheongju 28644, Republic of Korea
[5] Max Planck Institute for Astronomy, Königstuhl 17, D-69117 Heidelberg, Germany
[6] Department of Astronomy, The Ohio State University, 140 W. 18th Avenue, Columbus, OH 43210, USA
[7] Astronomical Observatory, University of Warsaw, Al. Ujazdowskie 4, 00-478 Warszawa, Poland
[8] Institute of Natural and Mathematical Sciences, Massey University, Auckland 0745, New Zealand
[9] University of Canterbury, Department of Physics and Astronomy, Private Bag 4800, Christchurch 8020, New Zealand
[10] University of Science and Technology, Korea, (UST), 217 Gajeong-ro, Yuseong-gu, Daejeon 34113, Republic of Korea
[11] Department of Particle Physics and Astrophysics, Weizmann Institute of Science, Rehovot 76100, Israel
[12] School of Space Research, Kyung Hee University, Yongin, Kyeonggi 17104, Republic of Korea
[13] Department of Physics, University of Warwick, Gibbet Hill Road, Coventry, CV4 7AL, UK
[14] Institute for Space-Earth Environmental Research, Nagoya University, Nagoya 464-8601, Japan
[15] NASA Goddard Space Flight Center, Code 667, Greenbelt, MD 20771, USA
[16] Department of Astronomy, University of Maryland, College Park, MD 20742, USA
[17] Department of Earth and Planetary Science, Graduate School of Science, The University of Tokyo, 7-3-1 Hongo, Bunkyo-ku, Tokyo 113-0033, Japan
[18] Instituto de Astrofísica de Canarias, Vía Láctea s/n, E-38205 La Laguna, Tenerife, Spain
[19] Department of Earth and Space Science, Graduate School of Science, Osaka University, Toyonaka, Osaka 560-0043, Japan
[20] Department of Physics, The Catholic University of America, Washington, DC 20064, USA
[21] Department of Astronomy, Graduate School of Science, The University of Tokyo, 7-3-1 Hongo, Bunkyo-ku, Tokyo 113-0033, Japan
[22] Sorbonne Université, CNRS, UMR 7095, Institut d'Astrophysique de Paris, 98 bis bd Arago, F-75014 Paris, France
[23] Department of Physics, University of Auckland, Private Bag 92019, Auckland, New Zealand
[24] University of Canterbury Mt. John Observatory, P.O. Box 56, Lake Tekapo 8770, New Zealand

Abstract

As a part of the "Systematic KMTNet Planetary Anomaly Search" series, we report five new planets (namely, OGLE-2016-BLG-1635Lb, MOA-2016-BLG-532Lb, KMT-2016-BLG-0625Lb, OGLE-2016-BLG-1850Lb, and KMT-2016-BLG-1751Lb) and one planet candidate (KMT-2016-BLG-1855), which were found by searching 2016 KMTNet prime fields. These *buried* planets show a wide range of masses from Earth-class to super-Jupiter-class and are located in both the disk and the bulge. The ultimate goal of this series is to build a complete planet sample. Because our work provides a complementary sample to other planet detection methods, which have different detection sensitivities, our complete sample will help us to obtain a better understanding of planet demographics in our Galaxy.

Unified Astronomy Thesaurus concepts: Gravitational microlensing exoplanet detection (2147)

1. Introduction

To build a complete microlensing planet sample, we conduct a series of works called "Systematic KMTNet Planetary Anomaly Search" based on a large microlensing survey archive obtained by the Korea Microlensing Telescope Network (KMTNet; Kim et al. 2016). We identify planet-like anomalies using the "Anomaly-Finder" algorithm (Zang et al. 2021, 2022a) instead of a traditional "by-eye" method, which can systematically identify almost all candidates showing anomalies on the light curve.[25] However, to reveal the origin of the anomaly requires (preliminary) models, including possible degenerate solutions to figure out the mass ratio of the lens component (i.e., q). Also, it requires investigating the data for the anomaly to check whether or not the anomaly is caused by a false-positive signal. Thus, detailed analyses for all anomalous events found by the AnomalyFinder require significant resources and human efforts.

Hence, for the KMTNet data obtained from 2016 to 2021, we conduct the work separately for each bulge season and for observing fields with different cadences, which are divided into prime (high cadence; $\Gamma = 2.0$–$4.0\,\mathrm{hr}^{-1}$) and subprime (low cadence; $\Gamma = 0.2$–$1.0\,\mathrm{hr}^{-1}$) fields. The KMTNet field information is described in Kim et al. (2018). Gould et al. (2022) introduced the systematic analysis of AnomalyFinder candidates. We have already done the systematic searches for the 2018 prime field (Gould et al. 2022; Hwang et al. 2022; Wang et al. 2022), 2018 subprime fields (Jung et al. 2022), 2019 prime fields (Zang et al. 2021, 2022a; Hwang et al. 2022), and 2019 subprime fields (Jung et al. 2023). In addition, Zang et al. (2023) presented a complete sample of planets with the mass ratio $q < 10^{-4}$ discovered from all candidate events observed from 2016 to 2019.

This is the ninth work to build the complete sample, which is conducted for the 2016 prime fields (i.e., BLG01, BLG41, BLG02, BLG42, BLG03, and BLG43). The AnomalyFinder algorithm and candidate review identified 106 anomalous events (plus 14 events that were already published). Based on visual inspection and/or preliminary modeling, 79 were eliminated as binaries. For the remaining 13 new candidates with at least one solution with $q < 0.06$, we re-reduce the photometry to check for/remove the systematics in the data sets. Based on further analysis with the best-quality data sets, seven were eliminated because they had no reliable planetary solutions (i.e., $q < 0.03$[26] with $\Delta\chi^2 < 10.0$. We also investigate one additional 2016 prime-field event for the detailed analysis, which was identified using the by-eye method and reported as a planet-like event but was not in the final AnomalyFinder candidate list (see Appendix B). Then, we find five new planets and one planet candidate based on detailed analyses: OGLE-2016-BLG-1635Lb, MOA-2016-BLG-532Lb, KMT-2016-BLG-0625Lb, OGLE-2016-BLG-1850Lb, KMT-2016-BLG-1751Lb, and KMT-2016-BLG-1855. We note that

these planetary systems are designated by the survey projects that first announced the events, as is traditional, even though the planetary systems were discovered based on the systematic search using the KMTNet data archive. We describe the observations of each survey in Section 2. Then, we describe the light-curve analysis for the planet candidates in Section 3. We note that, for the nine nonplanetary events, we report the analysis results in Appendix A for the record. In Section 4, we present analyses for the color–magnitude diagrams (CMDs) of the five planetary events. In Section 5, we present the properties of the planetary systems determined based on the Bayesian analyses. Lastly, we summarize the results of this work in Section 6.

2. Observations

In Tables 1 and 2 (see Appendix A), we present observational information for the anomalous events, which have at least one solution with $q < 0.06$ found from preliminary modeling. For the anomalous events, we gather all available data taken from microlensing surveys for preliminary modeling. The KMTNet pipeline data are available from the KMTNet Alert System (Kim et al. 2018; https://kmtnet.kasi.re.kr/~ulens/). They were obtained using three identical 1.6 m telescopes equipped with wide-field (4 deg^2) cameras. The telescopes are located at the Cerro Tololo Inter-American Observatory in Chile (KMTC), the South African Astronomical Observatory in South Africa (KMTS), and the Siding Spring Observatory in Australia (KMTA), which are in well-separated time zones to achieve near-continuous observations. Thus, the prime fields of the KMTNet have high cadences ($\Gamma \geqslant 2\,\mathrm{hr}^{-1}$) in the I band (Johnson–Cousins $BVRI$ filter system). Also, for the KMTC observations, KMTNet regularly takes one observation in the V band for every 10th I-band observation. We note that, for the KMTS observations, it takes one V-band observation for every 20th I-band observation.

The Optical Gravitational Lensing Experiment (OGLE; Udalski 2003; Udalski et al. 2015) data are available from the OGLE Early Warning System (Udalski et al. 1994; http://ogle.astrouw.edu.pl/ogle4/ews/ews.html) and were obtained using the 1.3 m Warsaw telescope with a 1.4 deg^2 camera located at Las Campanas Observatory in Chile. The OGLE observations were mainly made in the I band. Also, they periodically observe in the V band.

The Microlensing Observations in Astrophysics (MOA; Bond et al. 2001; Sumi et al. 2003) data are available on their alert system website (http://www.massey.ac.nz/~iabond/moa/alerts/) and were obtained using a 1.8 m telescope located at Mt. John University Observatory in New Zealand. The MOA observations were taken using the MOA-Red filter (hereafter referred to as the R band), which is roughly the sum of the Cousins R and I bands (wavelength ranges: 609–1109 nm; transmission ranges: 0.0–0.978).

The data of each survey were reduced by their own pipelines (KMTNet, Albrow et al. 2009; OGLE, Wozniak 2000; and MOA, Bond et al. 2001), which adopt/modify the difference image analysis technique (Tomaney & Crotts 1996; Alard & Lupton 1998). We note that, for the planet-like events listed in Tables 1 and 2, the KMTNet data are re-reduced using an optimized version of pySIS (H. Yang et al. 2023, in preparation) to obtain the best-quality data sets (hereafter tender loving care, TLC, reductions) for the analyses. Also, we reduce the V-band data to determine the source color using the

---

[25] Although the AnomalyFinder detects anomalies using criteria optimized to the KMTNet data, some anomalous events can be omitted because the criteria are not yet perfect. For example, AnomalyFinder missed KMT-2021-BLG-2294Lb (Shin et al. 2023). Thus, the by-eye method can help us to improve the criteria and understand the completeness of the final planet sample.

[26] The threshold of $q < 0.03$ as the definition of a planet is somewhat arbitrary, but no more so than a mass threshold of $M_{\mathrm{planet}} < 13\,M_{\mathrm{Jup}}$. Note that for $M_{\mathrm{host}} = 0.3\,M_\odot$, $q = 0.03$ corresponds to a planet mass $M_{\mathrm{planet}} \sim 10\,M_{\mathrm{Jup}}$. Considering that the majority of hosts in our Galaxy are M dwarfs, our threshold covers almost all planets (although, in some extreme cases, e.g., black hole hosts, the secondary would not be a planet).

Table 1
Observations of 2016 Planetary Events

Event			Location			Obs. Info.	
KMTNet	OGLE	MOA	R.A. (J2000)	Decl. (J2000)	(ℓ, b)	A_I	Γ (hr^{-1})
0269	**1635**	⋯	$17^h54^m01\overset{s}{.}22$	$-30°46'38\overset{''}{.}10$	$(-0\overset{\circ}{.}65, -2\overset{\circ}{.}51)$	1.82	2.0
0506	1749	**532**	$17^h57^m44\overset{s}{.}18$	$-29°06'25\overset{''}{.}60$	$(+1\overset{\circ}{.}20, -2\overset{\circ}{.}37)$	1.56	4.0
0625	⋯	⋯	$18^h05^m39\overset{s}{.}66$	$-27°13'36\overset{''}{.}70$	$(+3\overset{\circ}{.}70, -2\overset{\circ}{.}96)$	0.95	4.0
1307	**1850**	⋯	$17^h52^m00\overset{s}{.}18$	$-32°12'38\overset{''}{.}20$	$(-2\overset{\circ}{.}10, -2\overset{\circ}{.}86)$	2.01	4.0
1751	⋯	Avail.	$17^h53^m28\overset{s}{.}62$	$-32°09'06\overset{''}{.}52$	$(-1\overset{\circ}{.}89, -3\overset{\circ}{.}10)$	2.11	4.0
1855	⋯	⋯	$17^h50^m13\overset{s}{.}25$	$-29°12'26\overset{''}{.}39$	$(+0\overset{\circ}{.}29, -1\overset{\circ}{.}00)$	5.97	4.0

Note. Bold indicates the "discovery" name of each event.

Table 2
Observations of 2016 Nonplanetary Events

Event			Location			Obs. Info.	
KMTNet	OGLE	MOA	R.A. (J2000)	Decl. (J2000)	(ℓ, b)	A_I	Γ (hr^{-1})
0020	**0987**	⋯	$17^h56^m34\overset{s}{.}37$	$-27°59'31\overset{''}{.}99$	$(+2\overset{\circ}{.}04, -1\overset{\circ}{.}59)$	1.78	4.0
0106	⋯	**123**	$17^h54^m17\overset{s}{.}90$	$-28°55'15\overset{''}{.}74$	$(+0\overset{\circ}{.}99, -1\overset{\circ}{.}62)$	1.72	1.0
0157	**0558**	⋯	$17^h57^m45\overset{s}{.}40$	$-28°20'07\overset{''}{.}40$	$(+1\overset{\circ}{.}88, -1\overset{\circ}{.}98)$	1.61	4.0
0374	⋯	Avail.	$17^h54^m48\overset{s}{.}45$	$-30°59'04\overset{''}{.}42$	$(-0\overset{\circ}{.}74, -2\overset{\circ}{.}76)$	1.43	4.0
0425	**0185**	⋯	$17^h52^m35\overset{s}{.}43$	$-31°19'51\overset{''}{.}60$	$(-1\overset{\circ}{.}28, -2\overset{\circ}{.}52)$	2.24	4.0
0446	⋯	⋯	$17^h51^m52\overset{s}{.}02$	$-28°50'00\overset{''}{.}17$	$(+0\overset{\circ}{.}79, -1\overset{\circ}{.}12)$	3.13	4.0
1716	**1722**	555	$17^h55^m21\overset{s}{.}82$	$-30°42'36\overset{''}{.}90$	$(-0\overset{\circ}{.}44, -2\overset{\circ}{.}72)$	1.73	4.0
1863	**0974**	351	$18^h01^m23\overset{s}{.}99$	$-27°33'20\overset{''}{.}30$	$(+2\overset{\circ}{.}95, -2\overset{\circ}{.}29)$	1.41	4.0

Note. Bold indicates the "discovery" name of each event.

pyDIA package (Bramich et al. 2013; Albrow 2017). We also note that some events require re-reduced data obtained from the OGLE and MOA surveys for the detailed analyses. The MOA did not alert the KMT-2016-BLG-1751 and KMT-2016-BLG-0374 events. However, the events are located in the MOA fields. Therefore, the MOA team provided re-reduced data for these two events. Event OGLE-2016-BLG-1850 has a long baseline extending to the 2017 season. The OGLE team provided re-reduced data for this event including the long baseline.

3. Light-curve Analysis

3.1. Basics of the Analysis

We conduct a detailed analysis of 13 candidates with re-reduced data sets using the optimized pySIS package (H. Yang et al. 2023, in preparation). The analysis of the five planetary events and one planet candidate is presented in this section, and the remaining seven events are briefly presented in Appendix A. We follow the methodology of the light-curve analysis described in Shin et al. (2023). We briefly describe the analysis process, which consists of two steps, to present the terminology used in this work.

First, we conduct a grid search to find all possible solutions, in particular, local minima having planetary mass ratios (i.e., $q \lesssim 0.03$). For the grid search, we start from the static 2L1S case, i.e., without motions of the lenses or source (we treat the static model as a standard (STD) model), where nLmS indicates the number of lenses (n) and sources (m), respectively. To describe a microlensing light curve, the STD model requires seven parameters (t_0, u_0, t_E, s, q, α, and ρ_*), which are respectively defined as the time at the peak of the light curve,

impact parameter, Einstein timescale, projected separation between binary lens components in units of the angular Einstein radius (θ_E), mass ratio of the lens components (i.e., $q \equiv M_{\text{secondary}}/M_{\text{primary}}$), angle between the source trajectory and binary axis, and angular source radius (θ_*) scaled by θ_E (i.e., $\rho_* \equiv \theta_*/\theta_E$). We set ($s$, q) as grid parameters for the grid search. Because these are most sensitive parameters to describe anomalies on the light curve. The ranges of (s, q) are $\log_{10}(s) \in [-1.0, 1.0]$ and $\log_{10}(q) \in [-5.5, 1.0]$ with 100 grid points for each range. We optimize the five remaining parameters using a χ^2 minimizing method called the Markov Chain Monte Carlo algorithm (Doran & Müller 2004). We note that α is treated as a semi-grid parameter because it is also sensitive to describing the anomalies; we start 21 seeds for the α parameter within the range of $\alpha \in [0, 2\pi]$.

Second, once we find all plausible models, we refine the model parameters for all cases by allowing all parameters to freely vary within physically possible ranges. During this second process, we rescale the errors of the data sets based on the best-fit model to make each data point contribute $\chi^2 \sim 1.0$. The error rescaling procedure is described in Yee et al. (2012). Briefly, $e_R = k\sqrt{e_O^2 + e_S^2}$, where e_R is the rescaled error, k is the rescaling factor, e_O is the original error, and e_S is the systematics term.

Based on the STD models, we consider higher-order effects if the solutions have a high chance of detecting the effects. Specifically, we first consider the annual microlens parallax (APRX) effect (Gould 1992) if the models show relatively long timescales (i.e., $t_E \gtrsim 15$ days at least). Once we find the APRX effect, we also consider the lens-orbital (OBT) effect because the OBT may affect the APRX measurements. Lastly, in the cases where the APRX effect is detected, we test the "xallarap"

effect ("parallax" spelled backward; Griest & Hu 1992; Han & Gould 1997; Paczynski 1997; Poindexter et al. 2005), which reflects the accelerating orbital motion of the secondary source without its brightness contribution. Because the xallarap effect can mimic the APRX effect, the xallarap test is required to confirm the APRX measurements.

From the detailed analysis, we claim the detection of planetary systems if the fiducial solutions satisfy both detection criteria: the solution(s) should have (1) $q < 0.03$ and (2) $\Delta\chi^2 < 10$ compared to other nonplanetary solution(s).

Lastly, we note that, to indicate the degenerate solutions that we found, we follow the unified notation of the $s^\dagger$ formalism described in Hwang et al. (2022) and Ryu et al. (2022). Also, we can check our solutions using the formalism for validation. Here we briefly present the $s^\dagger$ formalism for the description of each event in the following sections.

The separations ($s_\pm^\dagger$) caused by major and minor images (Gould & Loeb 1992) are expected as

$$s_\pm^\dagger \equiv \frac{\sqrt{u_{anom}^2 + 4} \pm u_{anom}}{2},$$ (1)

where $u_{anom} = (\tau_{anom}^2 + u_0^2)^{1/2}$ is the offset of the source position from the host obtained from the scaled time offset from the peak of the light curve, $\tau_{anom} \equiv (t_{anom} - t_0)/t_E$. The expected $s_\pm^\dagger$ can be compared to the empirical results. The comparison depends on the type of anomaly shape and the number of solutions. In general, the "bump"-shaped anomaly caused by the major image perturbation should correspond to the $s_+^\dagger$ expectation, while the "dip"-shaped anomaly caused by the minor image perturbation should correspond to the $s_-^\dagger$ expectation. For the number of solutions (i.e., degenerate cases), if we have a unique solution, the empirical s should correspond to one of $s_\pm^\dagger$. If we have two degenerate solutions, such as $s_\pm$, the empirical solutions have a relation of

$$s^\dagger = \sqrt{s_+ s_-},$$ (2)

which should correspond to one of the $s_\pm^\dagger$ values. The α can also be predicted as

$$\tan\alpha = \frac{u_0}{\tau_{anom}}.$$ (3)

More specifically, $\alpha = \tan^{-1}(u_0/\tau_{anom}) + j\pi$, where $j = (0, 1)$ for (major, minor) images, and the range of $\tan^{-1}$ is defined as $[0, \pi]$. We note that the α expectation depends on the coordinate system of the modeling. Lastly, in the case of the dip-shaped anomaly, we can obtain the first-order approximation of the q values, i.e.,

$$q = \left(\frac{\Delta t_{dip}}{4t_E}\right)^2 \frac{s \sin^2\alpha}{u_{anom}} = \left(\frac{\Delta t_{dip}}{4t_E}\right)^2 \frac{s}{|u_0|}|\sin^3\alpha|.$$ (4)

We note that the predicted q generally matches the empirical q value within a factor of ~2. This expectation is useful for judging how valuable an event is to conduct a detailed analysis (i.e., whether or not it is a planetary event), even if the expectation could not be very accurate. The theoretical origins of the heuristic analysis and such degeneracies are described in Gaudi & Gould (1997), Griest & Safizadeh (1998), and Zhang & Gaudi (2022).

3.2. OGLE-2016-BLG-1635

The light curve of OGLE-2016-BLG-1635 (which we identified as KMT-2016-BLG-0269) exhibits a bump-shaped anomaly at HJD' = 7,624.6. In Figure 1, we present the light curve with degenerate (i.e., $s_\pm$) models. We also present the model parameters in Table 3. From a heuristic analysis, we find $\tau_{anom} = 0.023$ and $u_{anom} = 0.036$ based on $t_{anom} = 7624.60$, $t_0 = 7624.12$, $u_0 = 0.028$, and $t_E = 21$ days. As a result, we expect $s_-^\dagger = 0.98$ and $s_+^\dagger = 1.02$. The $s_-^\dagger$ is consistent with $s^\dagger = 0.99$ for our solutions. Although degenerate solutions exist, the mass ratios of both cases are less than 0.03, which implies that the companion is a planet by our formal definition.

The timescale of this event is about 21 days, which implies that there is a possibility of measuring the APRX considering the empirical criterion of $t_E \gtrsim 15$ days. Thus, we test the APRX models for this event. We find χ^2 improvements of $\Delta\chi^2 = 7.24$ and 9.96 for the s_- and s_+ cases, respectively. The $\Delta\chi^2$ values are too small to claim the APRX detection. Moreover, the APRX parameters are not converged for the s_- case. For the s_+ case, the APRX model favors values of $|\pi_E| > 10$ that are not reliable because they are caused by overfitting systematics at the baseline. Hence, we conclude that the STD models should be the fiducial solutions for OGLE-2016-BLG-1635. We can only measure the upper limits of ρ_* (i.e., 3σ ranges) because the source does not cross the caustic as shown in Figure 1.

3.3. MOA-2016-BLG-532

In Figure 2, we present the light curve of MOA-2016-BLG-532 (which we identified as KMT-2016-BLG-0506), which shows a clear deviation from the 1L1S model with a finite source. Although the anomaly is neither obviously bump-shaped nor dip-shaped, we find that the heuristic analysis is valid. It yields $\tau_{anom} = -0.032$ and $u_{anom} = 0.034$ from $t_{anom} = 7636.20$ and $t_E = 21$ days. Then, we expect $s_+^\dagger = 1.017$, which matches exactly with $s^\dagger = 1.017$ (derived from the modeling). The light curve can be well described by a 2L1S interpretation with both planet and binary cases (see light curves and geometries in Figure 2). In Table 4, we present the best-fit parameters. However, we find that the binary case shows worse fits by $\Delta\chi^2 = 20.62$ and 22.32 for the s_+ and s_- cases, respectively. The $\Delta\chi^2$ amounts are larger than our criterion to claim the planet detection. Although we conclude that this event is caused by a planetary lens system, we report both cases because the crucial part of the light curve (HJD' = 7,637.1–7,637.4) for clearly distinguishing between planet and binary solutions is not covered.

For this event, ρ_* is measured. The signal of the finite-source effect comes from the peak of the light curve, which cannot be properly described by the 1L1S interpretation (see the residual of Figure 2). The peak part can be described by 2L1S solutions (planet cases) by touching the cusp of the central caustic (see Figure 2). As a result, ρ_* is well measured.

We also test the APRX effect because of the relatively long timescale of the event (i.e., $t_E \sim 21$ days). We find χ^2 improvements of $\Delta\chi^2 = 21.57$ and 12.73 for the s_+ and s_- cases, respectively. However, the APRX fits show values too big for both cases, i.e., $|\pi_{E,N}| > 10$, which comes from overfitting systematics at the baseline. This fact implies that the APRX measurement is not reliable. Thus, we do not adopt the results of the APRX models.
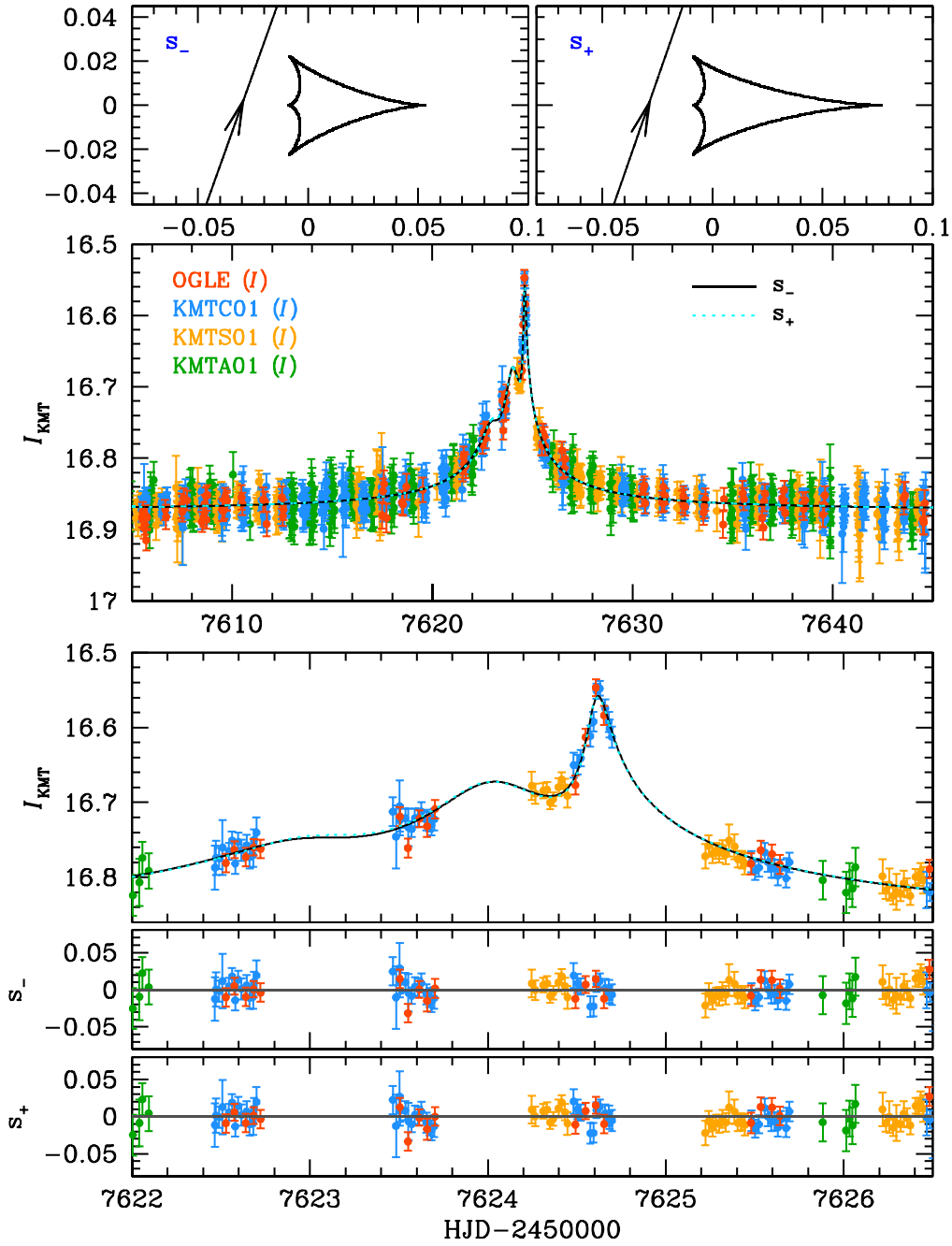
4

Figure 1. Light curve of OGLE-2016-BLG-1635 with $s_{\pm}$ models and their caustic geometries.

Table 3
Model Parameters of OGLE-2016-BLG-1635

Parameter	s_-	s_+
χ^2/N_{data}	5434.309/5436	5442.023/5436
t_0 [HJD′]	$7{,}624.124 \pm 0.013$	$7{,}624.118 \pm 0.014$
u_0	0.028 ± 0.004	0.028 ± 0.003
t_E [days]	20.908 ± 2.239	21.997 ± 2.252
s	0.587 ± 0.014	1.684 ± 0.043
q ($\times 10^{-4}$)	254.587 ± 33.644	247.586 ± 30.858
$\langle \log_{10} q \rangle$	-1.594 ± 0.058	-1.620 ± 0.056
α [rad]	5.056 ± 0.028	5.047 ± 0.030
$\rho_{*,\text{limit}}$	<0.0037	<0.0041

Note. HJD′ = HJD−2,450,000.0.

3.4. KMT-2016-BLG-0625

As shown in Figure 3, the light curve of KMT-2016-BLG-0625 shows a clear bump-shaped anomaly at HJD′ $\sim$ 7,662.95. Based on the heuristic analysis, we find $\tau_{\text{anom}} = 0.609$ and $u_{\text{anom}} = 0.613$ from $t_{\text{anom}} = 7662.95$ and $t_E = 11.5$ days. Then, we can expect that $s_-^{\dagger} = 0.739$ and $s_+^{\dagger} = 1.352$, which are consistent with $s_- = 0.741$ and $s_+ = 1.367$, respectively, among the solutions presented in Table 5. Also, we expect $\alpha = 0.12$ or 3.26 rad, which is consistent with $\alpha = 0.12$ and 3.22 for the s_+ and s_- cases, respectively.

As shown in Table 5, we find four planetary solutions ($s_{\pm}$ and $s_{\pm}'$) that can explain the anomaly. Because of the gaps near the anomaly, the $\Delta\chi^2$ values between the models (i.e.,
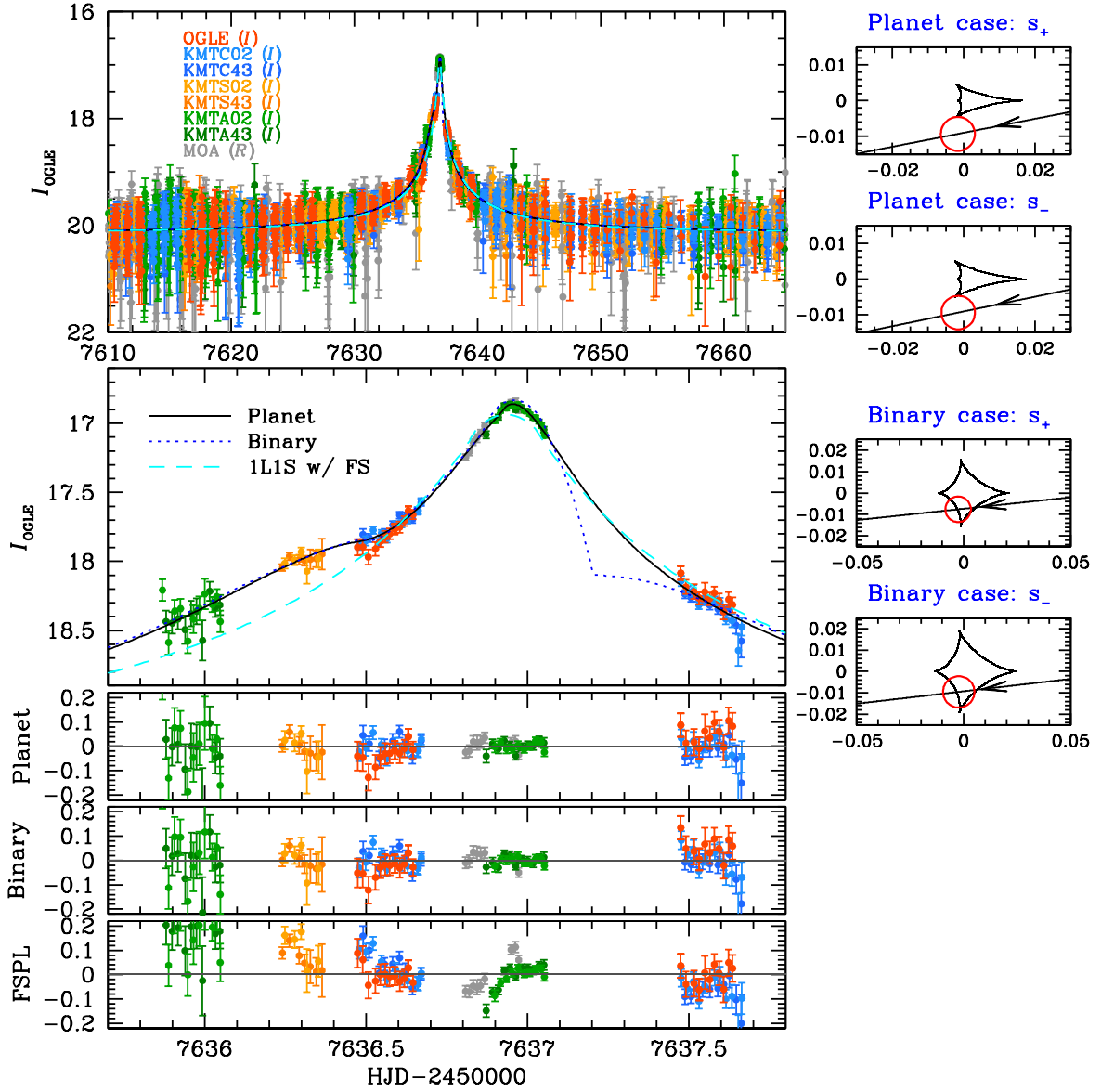
Figure 2. Light curve of MOA-2016-BLG-532 with the best-fit planetary model. We compare the planetary solution (black solid line) to the binary (blue dotted line) and 1L1S with finite-source (cyan dashed line) models. We also present caustic geometries of 2L1S models on the right side for comparison.

Table 4
Model Parameters of MOA-2016-BLG-532

Cases Parameter	Planet		Parameter	Binary	
	s_-	s_+		s_-	s_+
χ^2/N_{data}	**12,638.981/12,647**	**12,637.673/12,647**	$\Delta\chi^2_{binary-planet}$	22.322	20.619
t_0 [HJD′]	**7,636.877 ± 0.003**	**7,636.885 ± 0.003**	t_0 [HJD′]	7,636.934 ± 0.003	7,636.938 ± 0.003
u_0	**0.009 ± 0.001**	**0.009 ± 0.001**	u_0	0.009 ± 0.001	0.007 ± 0.001
t_E [days]	**20.786 ± 1.356**	**20.547 ± 1.491**	t_E [days]	21.606 ± 1.392	25.921 ± 1.427
s	**0.653 ± 0.018**	**1.584 ± 0.048**	s	0.278 ± 0.013	4.742 ± 0.362
q ($\times10^{-4}$)	**40.382 ± 5.534**	**40.441 ± 6.491**	q	0.156 ± 0.029	0.232 ± 0.062
$\langle\log_{10}q\rangle$	**−2.387 ± 0.058**	**−2.403 ± 0.070**	$\langle\log_{10}q\rangle$	−0.765 ± 0.073	−0.595 ± 0.100
α [rad]	**2.938 ± 0.008**	**2.949 ± 0.008**	α [rad]	3.026 ± 0.010	3.036 ± 0.008
ρ_* ($\times10^{-4}$)	**46.956 ± 3.995**	**47.591 ± 5.055**	ρ_* ($\times10^{-4}$)	73.386 ± 5.591	59.520 ± 3.267

Note. HJD′ = HJD–2,450,000.0. Bold indicates our fiducial solutions.

$\Delta\chi^2 = 0.98$–3.30) are too small to distinguish between them, although the model light curves show quite different features caused by the different caustic geometries presented in

Figure 4. Although we cannot break the degeneracy of the planetary solutions, all cases indicate that the companion of the lens system is a planet, i.e., $q = \mathcal{O}(10^{-4})$ (see Table 5).
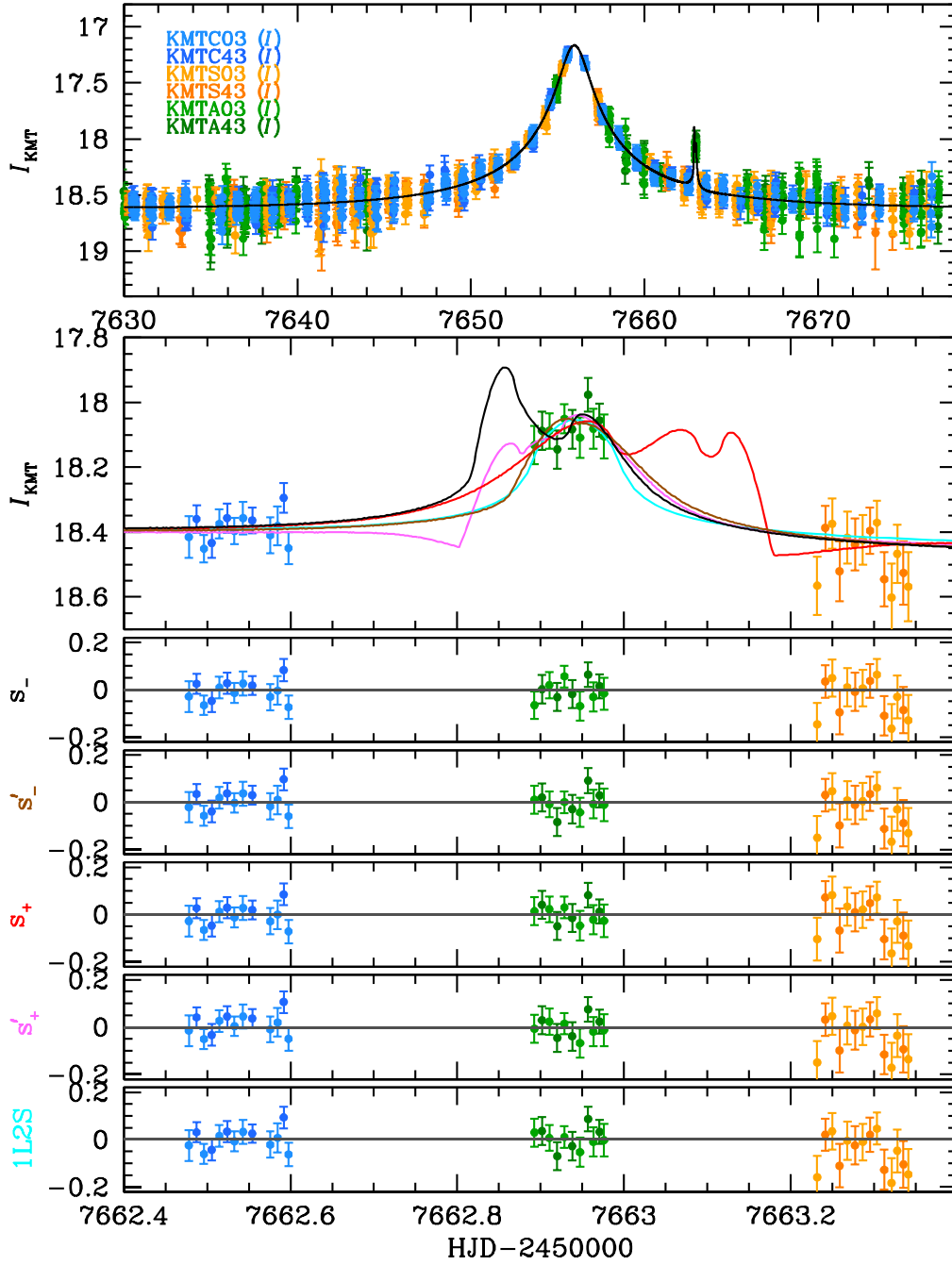
Figure 3. Light curve of KMT-2016-BLG-0625 with degenerate models.

Table 5
Model Parameters of KMT-2016-BLG-0625

Parameter	s_-	s_-'	s_+	s_+'	Parameter	1L2S
χ^2/N_{data}	8014.084/8021	8015.097/8021	8015.065/8021	8017.379/8021	χ^2/N_{data}	8021.432/8021
t_0 [HJD$'$]	$7{,}655.951 \pm 0.008$	$7{,}655.948 \pm 0.008$	$7{,}655.951 \pm 0.008$	$7{,}655.950 \pm 0.008$	t_{0,S_1} [HJD$'$]	$7{,}655.953 \pm 0.008$
u_0	0.073 ± 0.004	0.072 ± 0.004	0.075 ± 0.005	0.076 ± 0.004	u_{0,S_1}	0.078 ± 0.007
t_E [days]	11.494 ± 0.466	11.576 ± 0.466	11.335 ± 0.508	11.217 ± 0.405	t_E [days]	10.946 ± 0.491
s	0.741 ± 0.009	0.741 ± 0.009	1.367 ± 0.018	1.358 ± 0.015	t_{0,S_2} [HJD$'$]	$7{,}662.943 \pm 0.010$
q $(\times 10^{-4})$	2.357 ± 1.123	1.793 ± 1.048	0.727 ± 0.254	0.317 ± 0.173	u_{0,S_2} $(\times 10^{-4})$	3.751 ± 19.751
$\langle \log_{10} q \rangle$	-3.451 ± 0.130	-3.498 ± 0.136	-4.154 ± 0.159	-4.321 ± 0.159	$\cdots$	$\cdots$
α [rad]	3.217 ± 0.008	3.220 ± 0.008	0.122 ± 0.003	0.121 ± 0.002	q_{flux}	0.005 ± 0.001
ρ_* $(\times 10^{-4})$	12.256 ± 6.613	20.969 ± 7.334	17.498 ± 7.796	17.656 ± 7.383	ρ_{*,S_2} $(\times 10^{-4})$	51.309 ± 13.447

Note. HJD$'$ = HJD–2,450,000.0. We note that ρ_{*,S_1} is not measured for the 1L2S case. Only the upper limit (3σ range) can be measured: $\rho_{*,S_1} < 0.117$.
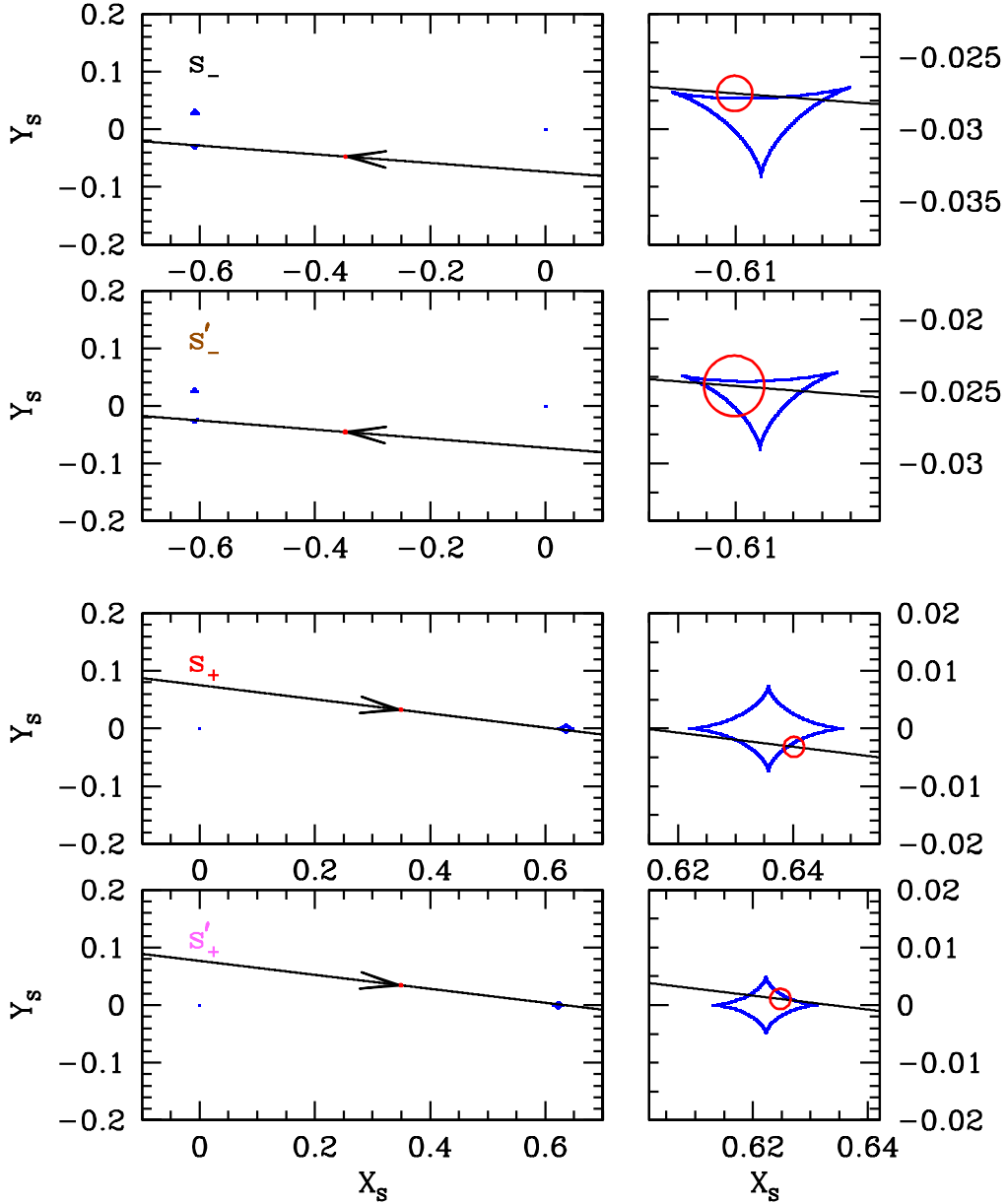
Figure 4. Caustic geometries of KMT-2016-BLG-0625 for the 2L1S models.

As shown in Figure 4, all planetary solutions produce the anomaly by crossing the caustic(s). As a result, we can measure the ρ_* despite the nonoptimal coverage. We do not test for the APRX measurement because of the relatively short timescale (i.e., $t_E \sim 11$ days).

Because the bump-type planetary anomaly can often lead to a 2L1S/1L2S degeneracy (Gaudi 1998), we check the 1L2S case for this event. In Table 5, we present the best-fit model of the 1L2S interpretation. We find that the 1L2S case is disfavored by $\Delta\chi^2 = 7.35$. However, the $\Delta\chi^2$ amount is not enough to conclusively resolve the 2L1S/1L2S degeneracy. Nevertheless, because we measure the ρ_* of the secondary source, we can measure the lens-source relative proper motion of the secondary source (μ_{rel,S_2}) to check the 1L2S model. We find (see Section 4) that $\mu_{\mathrm{rel},S_2} = 0.83 \pm 0.22$ mas yr^{-1}. By comparison, Gould (2022) found that for observed microlensing events with planetary-type anomalies, low proper motions

have probabilities

$$p(\leqslant\mu_{\mathrm{rel}}) = \frac{(\mu_{\mathrm{rel}}/2\sigma_\mu)^{\nu+1}}{[(\nu+1)/2]!} \rightarrow \frac{\mu_{\mathrm{rel}}^2}{4\sigma_\mu^2}$$

$$\rightarrow 2.8 \times 10^{-2}\left(\frac{\mu_{\mathrm{rel}}}{1 \text{ mas yr}^{-1}}\right)^2, \qquad (5)$$

where $\sigma_\mu = 3$ mas yr^{-1} and $\nu = 1$. See also Equation (9) of Jung et al. (2023). Applying this formula to the 1L2S solution, we find $p = 1.9\%$. This would, in itself, be a reasonably strong argument against the 1L2S solution. When combined with the fact that this solution is disfavored by $\Delta\chi^2 = 7.35$, we consider it to be decisive. Therefore, we reject the 1L2S solution and conclude that KMT-2016-BLG-0625 is caused by a planetary lens system. However, we note that the mass ratio q varies by a factor of ~ 3 over the four degenerate solutions.
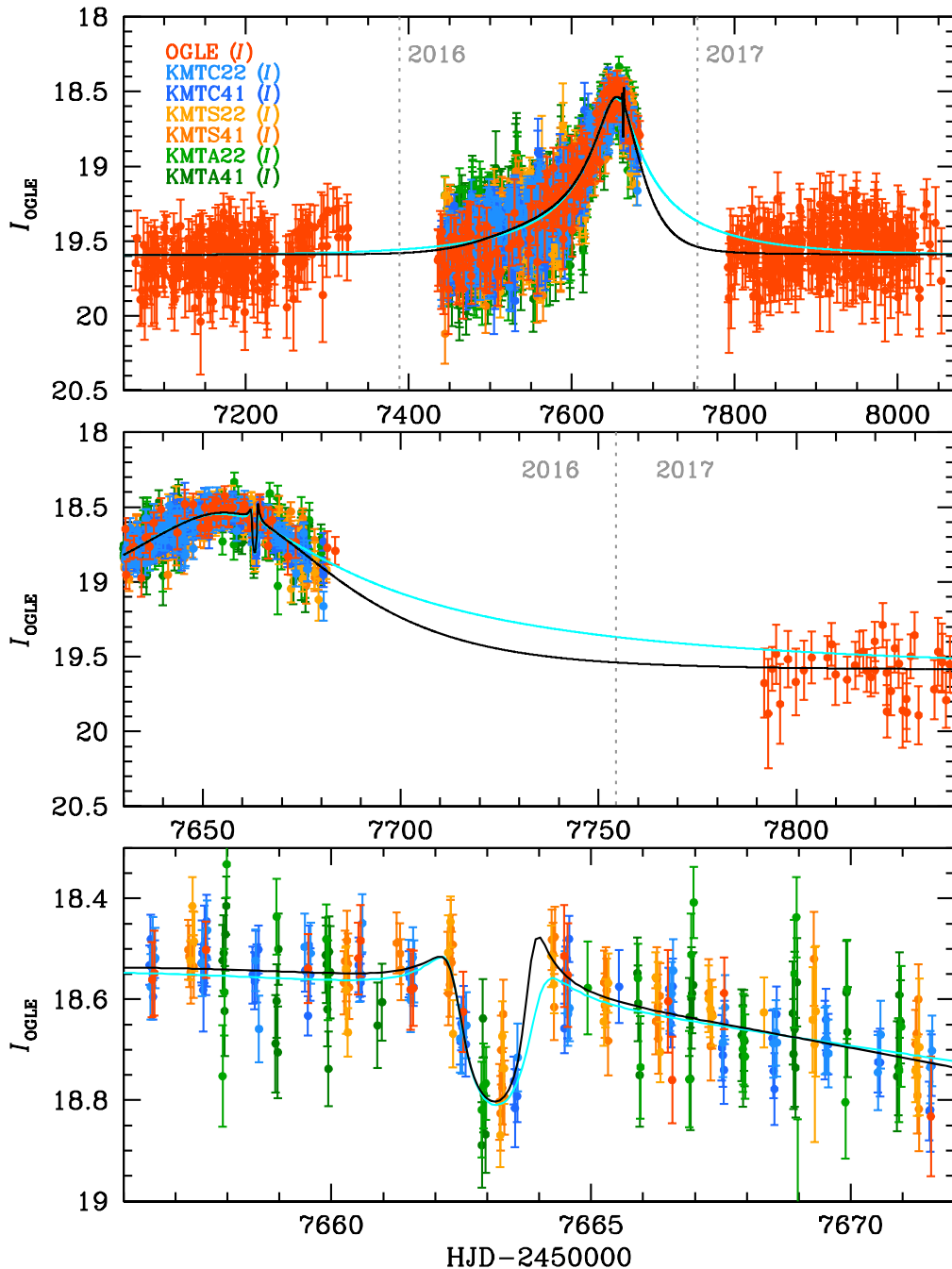
Figure 5. Light curve of OGLE-2016-BLG-1850 with STD (cyan) and APRX (black) models.

3.5. OGLE-2016-BLG-1850

The light curve of OGLE-2016-BLG-1850 (which we identified as KMT-2016-BLG-1307) shows a dip-shaped anomaly at HJD$' \sim 7{,}663$. Based on the heuristic analysis, we can expect $s^{\dagger}_{-} = 0.812$ and $q = 0.9 \times 10^{-4}$ (based on the $\tau_{\mathrm{anom}} = 0.126$ and $u_{\mathrm{anom}} = 0.419$ that are found from $t_{\mathrm{anom}} = 7663.15$ and $t_{\mathrm{E}} = 63.0$ days), which corresponds well with the empirical values: $s^{\dagger} = 0.813$ and $q \sim 1.0 \times 10^{-4}$.

In Figure 5, we present the observed light curve with zoom-ins of the anomaly. We also present the best-fit model light curves of the STD and APRX cases shown in Table 6. We find that both STD models (i.e., inner and outer cases) can describe the planetary anomaly as shown in Figure 6. However, the STD cases show a very long timescale ($t_{\mathrm{E}} \sim 210$ days), which

implies that the light curve is likely to be affected by a strong APRX effect. As expected, we find that the STD model cannot properly describe the 2017 baseline. Thus, we consider the ARPX effect. Then, we find a substantial χ^2 improvement of $\Delta\chi^2 \gtrsim 100$, which mostly comes from the better fit of the 2017 baseline (see Figure 5). Also, all APRX solutions can well describe the planetary anomaly as shown in Figure 6. In Figure 7, we present caustic geometries of all cases for comparison. We note that OGLE-2016-BLG-1850 is a non-caustic-crossing event. As a result, we cannot precisely measure ρ^* (only upper limits are available).

In Figure 8, we present the distributions of the APRX measurements, which are well converged. However, tests are required before we conclude that the APRX models should be
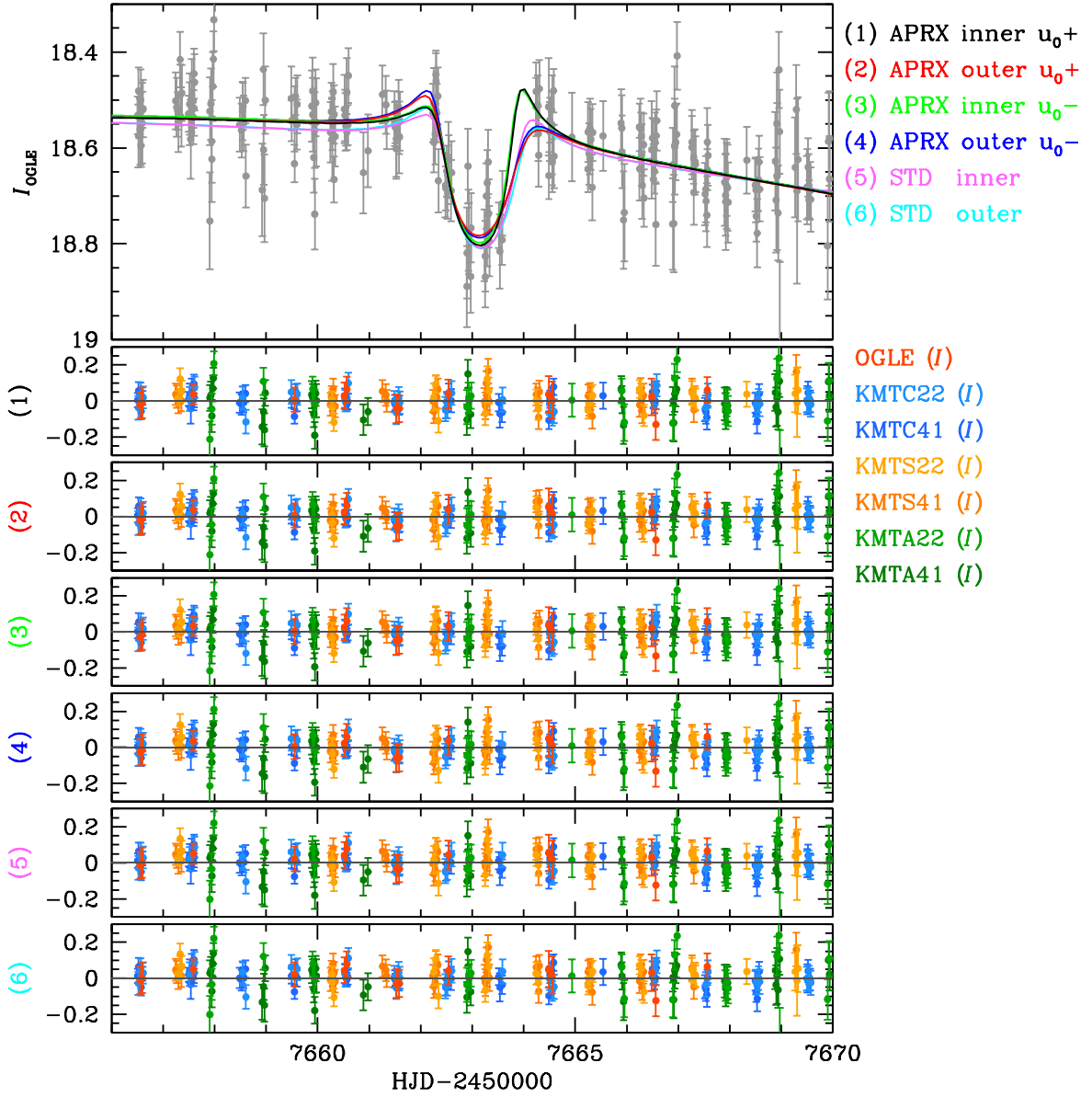
Figure 6. Zoom-in of the anomaly part of OGLE-2016-BLG-1850 for comparing all models with their residuals.

Table 6
Model Parameters of OGLE-2016-BLG-1850

Parameter	STD		APRX			
	Inner	Outer	Inner ($u_0 > 0$)	Outer ($u_0 > 0$)	Inner ($u_0 < 0$)	Outer ($u_0 < 0$)
$\chi^2/N_{\rm data}$	8108.940/7995	8108.800/7995	8004.449/7995	8006.818/7995	8007.775/7995	8009.766/7995
t_0 [HJD$'$]	$7{,}654.235 \pm 0.192$	$7{,}654.229 \pm 0.192$	$7{,}655.221 \pm 0.175$	$7{,}655.137 \pm 0.177$	$7{,}655.258 \pm 0.177$	$7{,}655.195 \pm 0.178$
u_0	0.106 ± 0.009	0.105 ± 0.010	0.401 ± 0.023	0.397 ± 0.020	-0.397 ± 0.020	-0.398 ± 0.031
$t_{\rm E}$ [days]	209.677 ± 16.086	211.183 ± 18.672	62.803 ± 3.843	63.190 ± 3.114	59.885 ± 2.917	60.581 ± 5.596
s	0.929 ± 0.005	0.961 ± 0.006	0.801 ± 0.010	0.826 ± 0.009	0.802 ± 0.008	0.825 ± 0.014
q ($\times 10^{-4}$)	0.416 ± 0.066	0.443 ± 0.068	1.009 ± 0.141	1.258 ± 0.161	1.072 ± 0.140	1.334 ± 0.180
$\langle \log_{10} q \rangle$	-4.378 ± 0.068	-4.366 ± 0.068	-3.983 ± 0.057	-3.923 ± 0.058	-3.945 ± 0.052	-3.890 ± 0.060
α [rad]	4.332 ± 0.011	4.329 ± 0.011	4.401 ± 0.012	4.394 ± 0.012	-4.385 ± 0.012	-4.384 ± 0.012
$\rho_{*,\rm limit}$	<0.003	<0.003	<0.007	<0.009	<0.007	<0.009
$\pi_{\rm E,N}$	$\cdots$	$\cdots$	0.075 ± 0.059	0.070 ± 0.060	0.095 ± 0.080	0.074 ± 0.084
$\pi_{\rm E,E}$	$\cdots$	$\cdots$	0.455 ± 0.037	0.441 ± 0.034	0.465 ± 0.035	0.449 ± 0.048

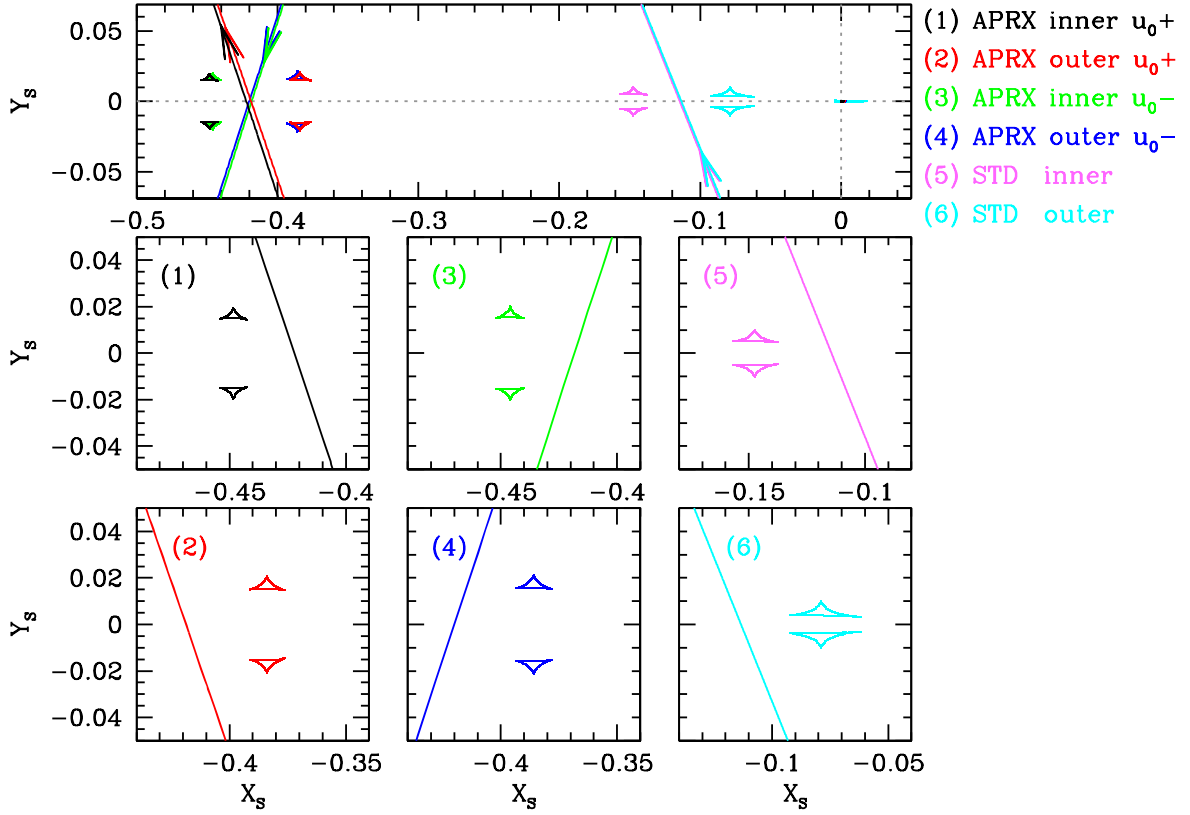**Note.** HJD$' =$ HJD$-2{,}450{,}000.0$.

Figure 7. Caustic geometries of OGLE-2016-BLG-1850.
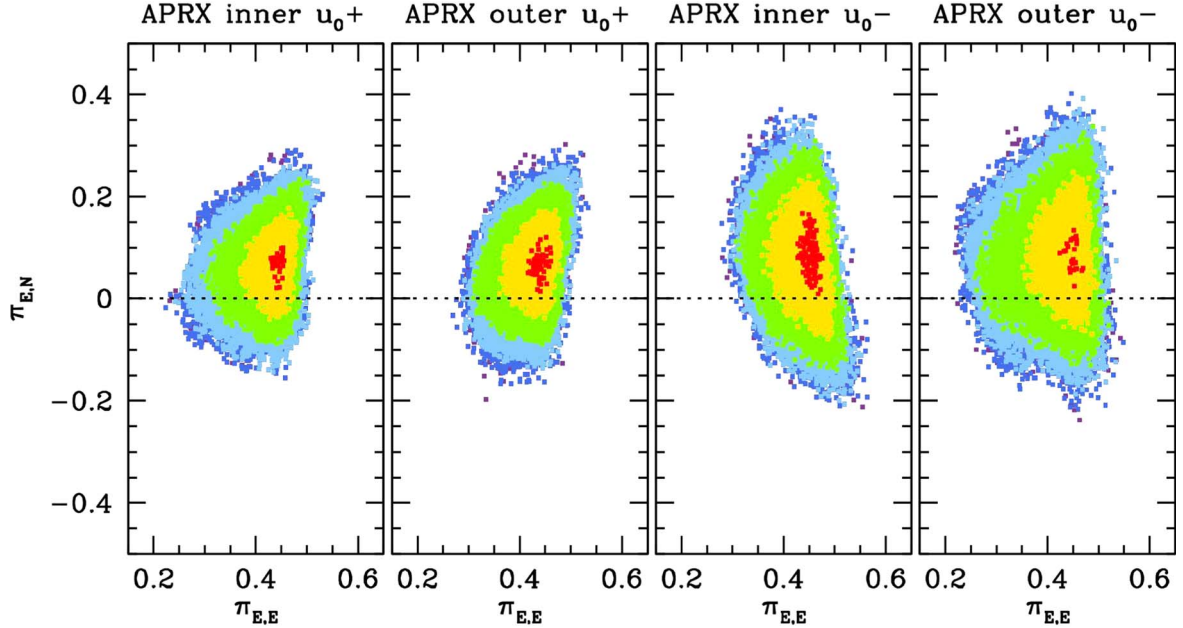

Figure 8. The APRX distributions of OGLE-2016-BLG-1850.

the fiducial solutions for this event. First, because the OBT motion can affect the APRX measurements (especially the uncertainty of the APRX measurement), we test the OBT effect. We conduct OBT+APRX models for each APRX case. We find that the OBT+APRX models show negligible χ^2 improvements of $\Delta\chi^2 \lesssim 0.5$ for the inner cases and $\Delta\chi^2 \lesssim 3.0$ for the outer cases. We also find that there is no effect on the uncertainties of the APRX measurements.

Second, to check the APRX models, we add xallarap to the models by introducing five parameters: the north and east components of the xallarap vector ($\xi_{E,N}$, $\xi_{E,E}$), the phase angle (ϕ), the inclination of the orbit (i), and the orbital period (P). We find that the xallarap cases show χ^2 improvements of $\Delta\chi^2 = 17.0$–22.1 compared to the APRX cases, which are marginal $\Delta\chi^2$ amounts to firmly claim that the xallarap models can be fiducial solutions for this event. Moreover, although the
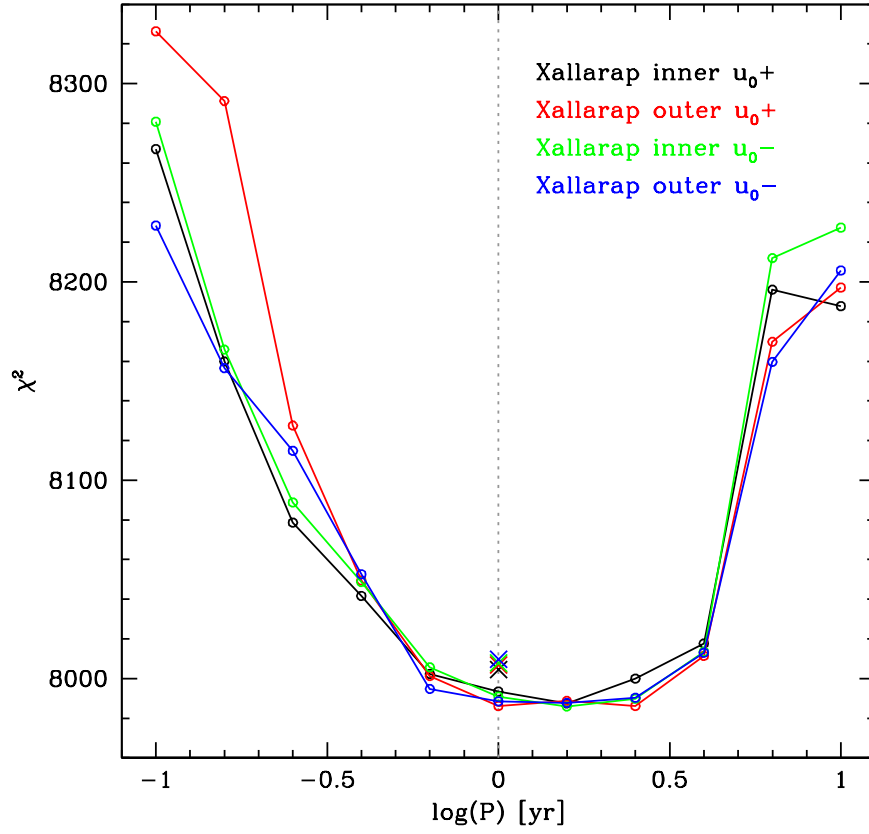
Figure 9. The $\log_{10}(P)$ and χ^2 plots of the xallarap models of OGLE-2016-BLG-1850. The crosses indicate the χ^2 of the APRX models.

best-fit model favors $\log_{10}(P) = 0.2$, as shown in Figure 9, we find that the xallarap models at $\log_{10}(P) = 0.0$ show $\Delta\chi^2 \lesssim 6.0$ compared to the best-fit xallarap model of each case. The clues imply that the asymmetry of the light curve is due to the APRX effect rather than the xallarap effect. Thus, we conclude that the fiducial solutions for this event are the APRX models.

3.6. KMT-2016-BLG-1751

In Figure 10, we present the observed light curve of KMT-2016-BLG-1751, which shows a clear planetary anomaly (i.e., dip feature) at the peak of the light curve. Based on the heuristic analysis ($\tau_{\rm anom} \sim 0.00$ and $u_{\rm anom} = 0.11$ from $t_{\rm anom} = 7501.00$ and $t_{\rm E} = 10.0$ days), we expect $s_-^\dagger = 0.946$, which is well matched to both $s^\dagger = \sqrt{s_- s_+} = 0.944$ and $s^\dagger = \sqrt{s_-' s_+'} = 0.947$. We also expect $q \simeq 0.003$ (for both $s^\dagger$ cases), which agrees with the q values presented in Table 7 to within a factor of ~ 2.

We find that several solutions can explain the anomaly because the coverage of the anomaly (HJD$' = 7,500.8$–$7,502.4$) is nonoptimal. Thus, despite including MOA data, the gap in the anomaly produces degenerate solutions. In Table 7, we present model parameters of the solutions. In Figures 11 and 12, we also present the s–q parameter space with the locations of each solution and their caustic geometries. The competing solutions show relatively small $\Delta\chi^2$ values compared to the best-fit solution (i.e., s_+ case): 8.53, 5.70, 8.78, and 10.78 for the s_+', s_-, s_-', and s_-'' cases, respectively. For the $s_\pm$ and $s_\pm'$ cases, we obtain a best-fit value for ρ_*. However, as might be expected from the geometries, we find that the measurements are consistent with zero at 3σ. Thus, in these cases, we effectively have only an upper limit on ρ_*, so we will apply a

ρ_* weight function in the Bayesian analysis in Section 5. For the s_-'' case, ρ_* is measured from the caustic crossing. However, the s_-'' solution does not satisfy our χ^2 criterion (i.e., $\Delta\chi^2 < 10.0$). Thus, we remove the s_-'' case from our fiducial solutions for determining the lens properties of this event. However, because the $\Delta\chi^2$ of this case is very close to the χ^2 criterion, we present the parameters and figures of this solution for completeness. Lastly, because of the short timescale (i.e., $t_{\rm E} \sim 10$ days), we do not conduct the APRX modeling for this event.

3.7. KMT-2016-BLG-1855

In Figure 13, we present the observed light curve of KMT-2016-BLG-1855 with the best-fit model curve and caustic geometry. The observed light curve exhibits anomalies at the peak. We find that the anomaly can be described by a source approaching a diamond-shaped central caustic, which is in the regime of a Chang–Refsdal (C-R) lens (Chang & Refsdal 1979). The best-fit model shows $\frac{1}{q} = 0.023 \pm 0.012$, which satisfies our mass-ratio criterion to claim planet detection. However, we find that there are possible solutions caused by the close/wide (Griest & Safizadeh 1998), offset (Zhang & Gaudi 2022; Zhang et al. 2022b), and 2L1S/1L2S (Gaudi 1998) degeneracies. We also check for the α-degeneracy (i.e., the degeneracy caused by the angle of the source trajectory), which can occur for C-R lenses. These solutions are denoted $n(\pi/2)$, where $n = (1, 2, 3)$. In Tables 8 and 9, we present model parameters of the best-fit and degenerate models. In Figures 14 and 15, we present all possible solutions with their caustic geometries and residuals for comparison.
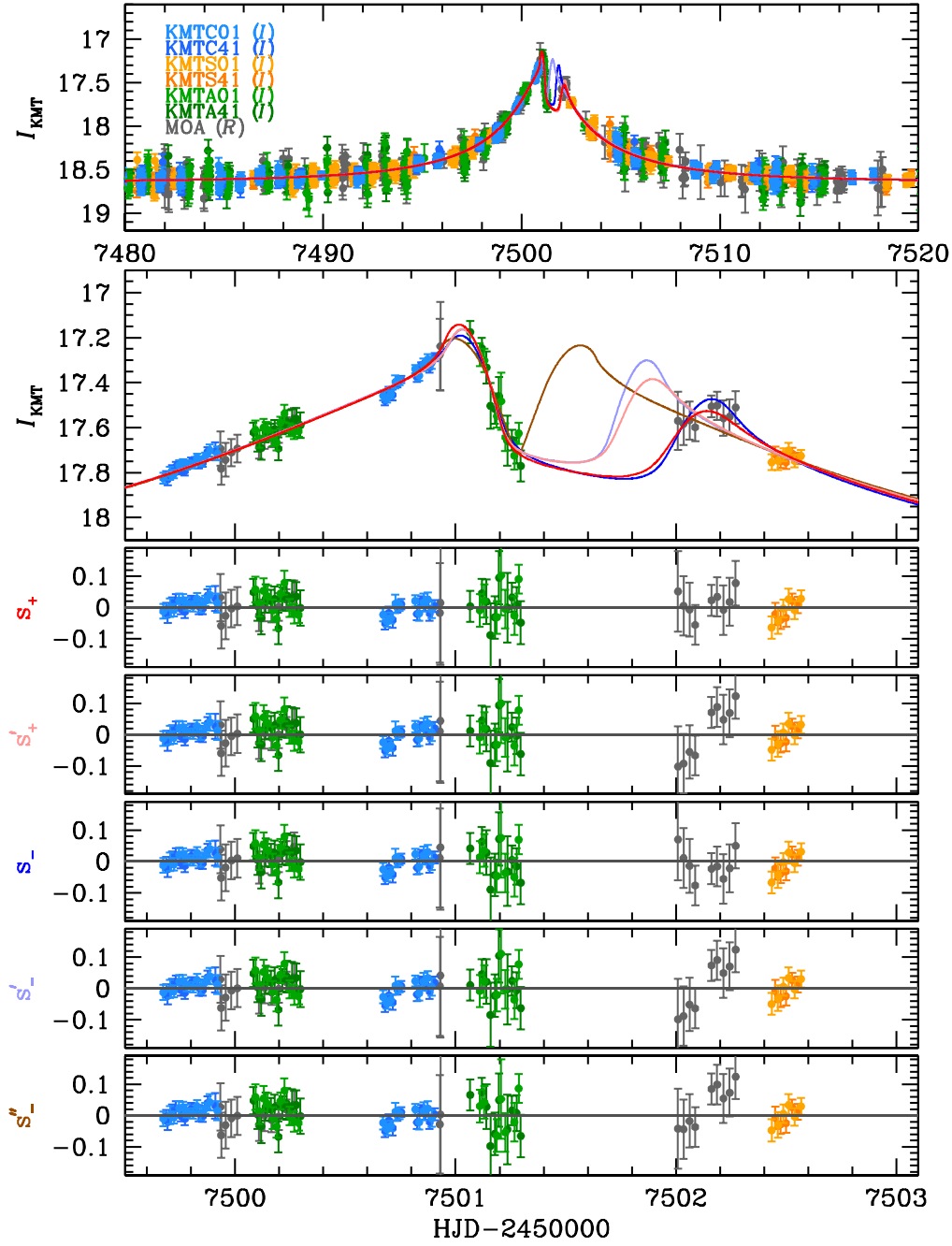
Figure 10. Light curve of KMT-2016-BLG-1751 with degenerate models.

Table 7
Model Parameters of KMT-2016-BLG-1751

Parameter	s_+	s_+'	s_-	s_-'	s_-''
χ^2/N_{data}	**8995.960/8994**	**9004.487/8994**	**9001.658/8994**	**9004.738/8994**	9006.742/8994
t_0 [HJD′]	**7,501.132 ± 0.016**	**7,501.187 ± 0.021**	**7,501.106 ± 0.017**	**7,501.176 ± 0.019**	7,501.214 ± 0.016
u_0	**0.113 ± 0.005**	**0.111 ± 0.005**	**0.107 ± 0.005**	**0.110 ± 0.005**	0.103 ± 0.006
t_E [days]	**9.625 ± 0.293**	**9.475 ± 0.292**	**9.997 ± 0.301**	**9.469 ± 0.284**	9.591 ± 0.298
s	**1.050 ± 0.014**	**1.027 ± 0.017**	**0.848 ± 0.011**	**0.873 ± 0.015**	0.950 ± 0.007
q (×10^{-4})	**64.992 ± 4.479**	**39.995 ± 8.312**	**61.147 ± 3.556**	**38.161 ± 7.169**	7.207 ± 2.902
$\langle \log_{10} q \rangle$	**−2.200 ± 0.031**	**−2.447 ± 0.113**	**−2.212 ± 0.025**	**−2.485 ± 0.104**	−3.036 ± 0.130
α [rad]	**4.339 ± 0.022**	**4.470 ± 0.049**	**4.318 ± 0.021**	**4.467 ± 0.044**	4.643 ± 0.035
$\rho_{*,\text{limit}}$	**<0.019**	**<0.020**	**<0.021**	**<0.020**	...
ρ_*	...	...	...	...	0.019 ± 0.002

Note. HJD′ = HJD–2,450,000.0. Bold indicates our fiducial solutions.
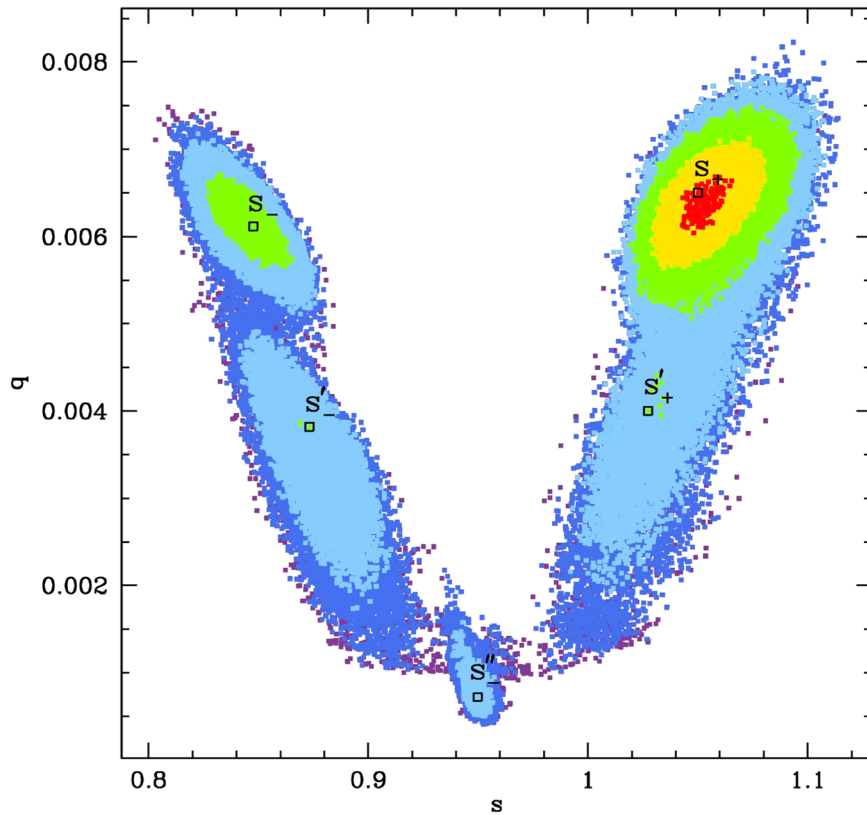
13

Figure 11. The s–q parameter space of KMT-2016-BLG-1751 showing possible solutions.

We find a total of seven degenerate solutions including the 1L2S case. For the 2L1S cases, we find the initial parameters of the A, B, C, and D solutions based on the grid search. We also find initial parameters for their paired offset-degeneracy solutions (i.e., A′, B′, C′, and D′) using heuristic analysis: $s' = (s_{\pm}^{\dagger})^2/s_{\pm}$, where subscripts $+$ and $-$ indicate the $s > 1$ and $s < 1$ cases, respectively. Note that we transform our coordinate system from "secondary" to "primary" components to conduct the heuristic analysis because the analysis is valid for the primary coordinate system. Then, we refine the model parameters to check the degeneracy (note that we restore the coordinates for direct comparison).

For the A and A′ pair, the heuristic analysis predicts $s' = 3.680$. The paired offset-degeneracy solution of the A case (i.e., A′) is consistent with the $3(\pi/2)$ C-R case, which has an empirical value of $s = 3.780 \pm 0.088$. This A family degeneracy can be resolved (see below). For the B and B′ pair, the heuristic analysis predicts $s' = 3.600$, which is consistent with the empirical $s = 3.708 \pm 0.121$ from the B′ case. This B family is a C-R lensing case, which shows large uncertainties in the set of (t_E, s, q) parameters. For the C and C′ pair, the heuristic analysis predicts $s' = 1.162$, which is consistent with the empirical value of $s = 1.161 \pm 0.042$ from the C′ case. Indeed, the C family is caused by close/wide degeneracy. For the D case, the heuristic analysis expects $s' = 2.951$. However, we find that the paired offset solution evolves toward the B case. Indeed, the caustic geometry of the D case is asymmetric, which is different from the C-R lens case. Thus, because the source trajectory is not perpendicular to the binary axis, the paired solution from the heuristic analysis cannot describe the peak of the light curve, and we would not necessarily expect it to (Gaudi & Gould 1997). In all cases, the ρ_* measurements are

uncertain and give only upper limits of ρ_* values, as expected from non-caustic-crossing geometries.

All of the 2L1S models nominally have long timescales (t_E), but they also have $q > 1.0$ (i.e., they approach the secondary, less massive lens component). For these cases, the actual timescale (t_E') of the event should be scaled by $t_E' = t_E \sqrt{q}$ as shown in Tables 8 and 9. Hence, given that $t_E' \sim 15$ days, it is not surprising that we do not detect the APRX effect (i.e., $\Delta\chi^2_{\text{STD−APRX}} = 2.7$). Thus, we conclude that the STD models are the fiducial solutions for this event.

As shown in Figures 14 and 15, all cases describe the peak anomaly well. Although they nominally have $\Delta\chi^2 > 10$ compared to the best-fit case, we find that the χ^2 differences mostly come from the baseline part (HJD′ $> 7,600$). The best-fit case has a wide caustic, which creates a very shallow bump peaking at HJD′ $\sim 7,717$, $\Delta I \sim 0.01$ mag above the baseline observations (see the blue dashed line shown in Figure 13). However, systematics may exist in the baseline data at this level, especially considering the dispersion of the baseline data (i.e., $\Delta I \sim 0.65$ mag). Thus, we compute $\Delta\chi^2$ without the baseline data of HJD′ $> 7,600$ (i.e., $t_0 + 1.5\,t_E \sim 7595.25$) because the χ^2 contributions at the baseline cannot be considered reliable. After this cut, the $\Delta\chi^2$ values for all cases (except the A′ case) are less than 9, as shown in Tables 8 and 9. Hence, we cannot claim to resolve most degenerate solutions.

The 1L2S model is completely degenerate with the 2L1S models and cannot be excluded based on physical considerations. First, the finite-source effect is not measured; the ρ_* distributions of both sources reach zero within 3σ. Moreover, because of the severe extinction ($A_I = 5.97$; Gonzalez et al. 2012), additional information to conclusively resolve the
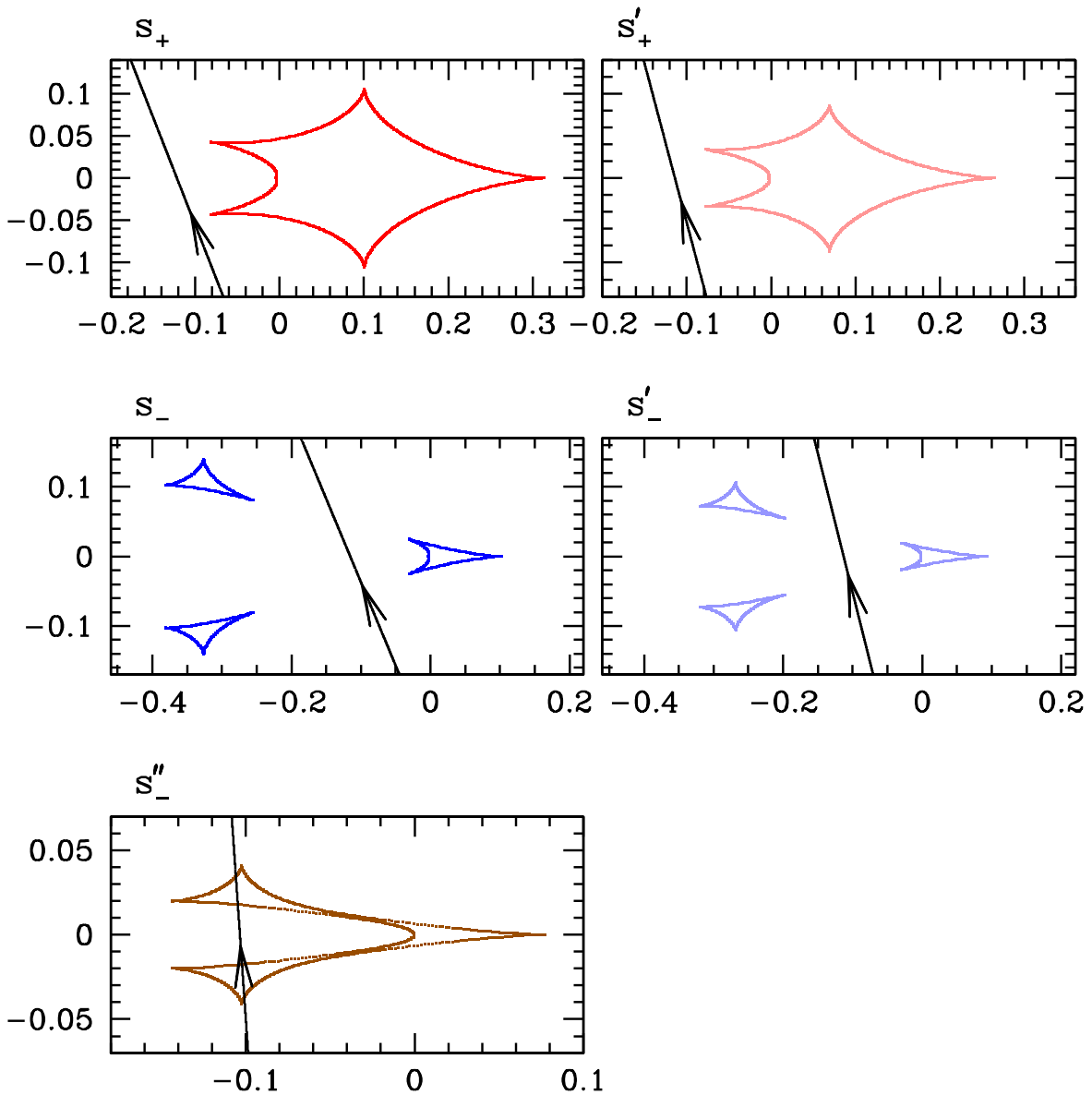
Figure 12. Caustic geometry of each solution of KMT-2016-BLG-1751. The color of the caustic is identical to the color of the light curve shown in Figure 10.

degeneracy, such as the source color (see Section 4), is not available for this event.

Thus, we treat KMT-2016-BLG-1855 as a planet candidate, and we strongly counsel against cataloging it as a planet.

4. CMD Analysis

For the five planetary events, we measure the angular source radius (θ_*) using the conventional method described in Yoo et al. (2004), i.e., the CMD analysis. The θ_* measurement is important. If we measure ρ_* from the finite-source effect, we can determine $\theta_E = \theta_*/\rho_*$. Furthermore, even if we cannot measure ρ_*, θ_* is required to apply the ρ_* distributions as constraints on the Bayesian analysis.

We proceed with this analysis based on multiband observations (I and V bands) taken from the KMTNet survey (i.e., KMTC). We align the KMTNet instrumental color and magnitudes to the OGLE-III scales using cross-matching of field stars. We note that the position of the red giant clump centroid (RGC) is determined based on the OGLE-III CMD

(Szymański et al. 2011). In Figure 16, we present CMDs of the five planetary events for the best-fit cases with the positions of the RGC, source, and blend. We also present all information from the CMD analysis, including θ_*, θ_E, and $\mu_{\rm rel}$, in Table 10. We note that the intrinsic color of the RGC is adopted from Bensby et al. (2011). The dereddened magnitude of the RGC is adopted from Nataf et al. (2013). The dereddened colors and magnitudes of the source and blend are determined by assuming they experienced the same amount of stellar extinction of the RGC. Lastly, we determine θ_* using the surface brightness–color relation adopted from Kervella et al. (2004).

Note that we proceed differently for the special case of the putative second source in the 1L2S solution for KMT-2016-BLG-0625. We find $I_{\rm S,0} = 19.345 \pm 0.010$ using the method of Yoo et al. (2004). Then, we derive $I_{\rm S_2,0} = 25.112 \pm 0.231$ based on the $q_{\rm flux}$ value of the 1L2S model. We convert the dereddened I-band magnitude of the second source to its absolute I-band magnitude (M_I) by adopting $M_{I,\rm RGC} = -0.12 \pm 0.09$ and $I_{\rm RGC,0} = 14.335$ from Nataf et al. (2013):
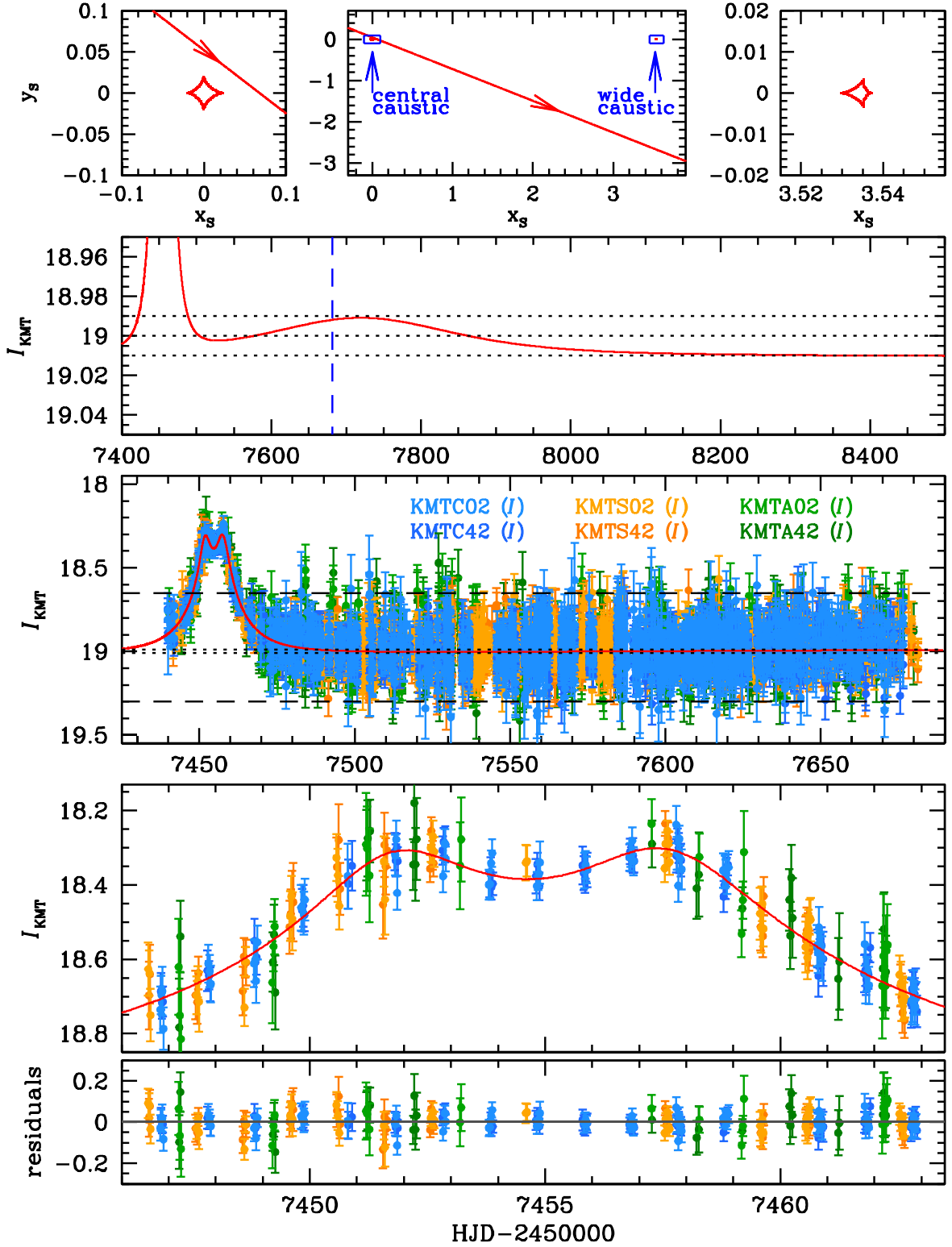
Figure 13. Light curve of KMT-2016-BLG-1855 with the best-fit model.

$M_{I,S_2} = 10.656 \pm 0.248$. We can estimate the radius of the second source, $R_{S_2} \sim 0.208\,R_\odot$, based on studies of stellar properties (Pecaut et al. 2012; Pecaut & Mamajek 2013). Thus, we find that the angular radius of the second source is $\theta_{*,S_2} \sim 0.128\,\mu$as, which yields $\mu_{\mathrm{rel},S_2} = 0.83 \pm 0.22$ mas yr^{-1}. Note that we adopt the distance to the second source ($D_{S_2} \sim 7.59$ kpc) from Nataf et al. (2013).

For KMT-2016-BLG-1855, the field is highly extincted ($A_I = 5.97$; Gonzalez et al. 2012), so it is not possible to measure the source color in the V band from the KMTNet data. We construct an $I - H$ CMD for this event by cross-matching the OGLE-III catalog (Szymański et al. 2011) to the VVV DR2 (Minniti et al. 2017), and we convert the KMT pyDIA I magnitude of the source to the OGLE-III system. This suggests

Table 8
Model Parameters of KMT-2016-BLG-1855

Parameter	A: Best Fit	A′: 3(π/2)	B: 2(π/2)	B′: 2(π/2)
$\chi^2/N_{\rm data}$	**7734.217/7735**	7749.828/7735	7758.514/7735	7757.884/7735
$\Delta\chi^2$ (full data)	...	15.611	24.297	23.667
$\Delta\chi^2$ (HJD′ < 7600)	...	13.196	8.055	8.821
t_0 [HJD′]	**7,454.015 ± 0.080**	7,455.619 ± 0.078	7,453.981 ± 0.104	7,455.694 ± 0.086
u_0	**0.041 ± 0.007**	0.040 ± 0.006	0.001 ± 0.001	−0.001 ± 0.001
$t_{\rm E}$ [days]	**94.156 ± 17.078**	103.244 ± 18.364	2889.644 ± 493.547	2924.318 ± 120.251
$t'_{\rm E}$ [days]	**14.424 ± 0.908**	15.331 ± 0.904	13.282 ± 0.984	13.321 ± 0.945
s	**3.798 ± 0.108**	3.780 ± 0.088	3.598 ± 0.132	3.708 ± 0.121
q	**42.614 ± 21.193**	45.352 ± 24.063	$(47.334 ± 11.658) \times 10^3$	$(48.189 ± 5.978) \times 10^3$
$\frac{1}{q}$	**0.023 ± 0.012**	0.022 ± 0.009	$(0.211 ± 0.419) \times 10^{-4}$	$(0.208 ± 0.042) \times 10^{-4}$
$\langle \log_{10} \frac{1}{q} \rangle$	**−1.605 ± 0.196**	−1.666 ± 0.173	−4.249 ± 0.248	−4.574 ± 0.068
α [rad]	**0.657 ± 0.012**	5.603 ± 0.016	3.812 ± 0.016	3.803 ± 0.015
$\rho_{*,\rm limit}$	**<0.023**	<0.024	<0.002	<0.0006

Note. HJD′ = HJD–2,450,000.0. Bold indicates the best-fit solution.

Table 9
Model Parameters of KMT-2016-BLG-1855 (Continued)

Parameter	C: s'_-	C′: s'_+	D: 1(π/2)	Parameter	E: 1L2S
$\chi^2/N_{\rm data}$	7751.738/7735	7750.972/7735	7755.555/7735	$\chi^2/N_{\rm data}$	7752.925/7735
$\Delta\chi^2$ (full data)	17.521	16.775	21.338	$\Delta\chi^2$ (full data)	18.708
$\Delta\chi^2$ (HJD′ < 7600)	2.269	1.414	5.727	$\Delta\chi^2$ (HJD′ < 7600)	3.060
t_0 [HJD′]	7,454.864 ± 0.061	7,454.893 ± 0.090	7,455.816 ± 0.102	t_{0,S_1} [HJD′]	7,451.870 ± 0.112
u_0	0.226 ± 0.049	0.531 ± 0.066	0.148 ± 0.024	u_{0,S_1}	0.124 ± 0.015
$t_{\rm E}$ [days]	15.382 ± 1.392	15.408 ± 1.392	24.015 ± 4.242	$t_{\rm E}$ [days]	17.409 ± 1.362
$t'_{\rm E}$ [days]	...	...	14.176 ± 1.999	t_{0,S_2} [HJD′]	7457.697 ± 0.106
s	0.687 ± 0.025	1.161 ± 0.042	3.392 ± 0.162	u_{0,S_1}	0.133 ± 0.018
q	18.911 ± 3.028	16.223 ± 2.143	2.870 ± 1.418	$q_{\rm flux}$	1.146 ± 0.181
$\frac{1}{q}$	0.053 ± 0.006	0.062 ± 0.007	0.348 ± 0.215	...	...
$\langle \log_{10} \frac{1}{q} \rangle$	−1.328 ± 0.059	−1.229 ± 0.053	−0.389 ± 0.203	...	...
α [rad]	1.582 ± 0.013	1.578 ± 0.012	2.544 ± 0.014	...	...
$\rho_{*,\rm limit}$	<0.168	<0.178	<0.101	...	...

Note. HJD′ = HJD–2,450,000.0.

that the source is a red clump giant. However, the clump is extended in both color and magnitude in the CMD. Both the lack of a color measurement and the uncertainty in the clump magnitude would make $\theta_\star$ highly uncertain. However, there are no meaningful constraints on $\rho_\star$, so we do not calculate a value for $\theta_\star$ because it has no bearing on the analysis.

We also measure the astrometric offsets between baseline objects and sources. Because we can use the blend light as a constraint for the Bayesian analysis if the blend light is associated with the lens. For all planetary events, we find that the blend is separated by $>0\overset{''}{.}3$, so it is dominated by a star that is not the lens.

5. Planet Properties

5.1. Bayesian Formalism

To determine the lens properties, two additional observables are simultaneously required. They are the angular Einstein ring radius ($\theta_{\rm E}$) and the amplitude of the microlens parallax vector ($|\pi_{\rm E}|$), which are measured from the effects of the finite source and microlens parallax, respectively. However, the events for which both observables are simultaneously measured are relatively rare. Indeed, we can measure only one of these observables out of five planetary events presented in this work. Thus, we estimate the lens properties using the Bayesian analysis. We follow the Bayesian formalism described in Shin et al. (2023) to generate the Galactic prior. Then, we apply the measured observable as a constraint on the Galactic prior. In Table 11, we present the applied constraints and lens properties for each event. For the notation of the constraint, $t_{\rm E}$ indicates a Gaussian weight function constructed based on the best-fit value of the $t_{\rm E}$ parameter and its uncertainty, $\theta_{\rm E}$ indicates the Gaussian weight adopted from the measured $\theta_{\rm E}$ if $\rho_\star$ is certainly measured, and $\rho_\star$ indicates a weight function built based on the $\Delta\chi^2$ distribution as a function of $\rho_\star$ if the $\rho_\star$ measurement is uncertain. Lastly, $\pi_{\rm E}$ indicates a constraint using the 2D APRX distributions described in Ryu et al. (2019). In Table 11, we present various lens properties for each event because each event has degenerate solutions, which yield different lens properties. For ease of cataloging, we present "adopted" values for each property by adopting the method described in Jung et al. (2023), i.e., weighted average values.
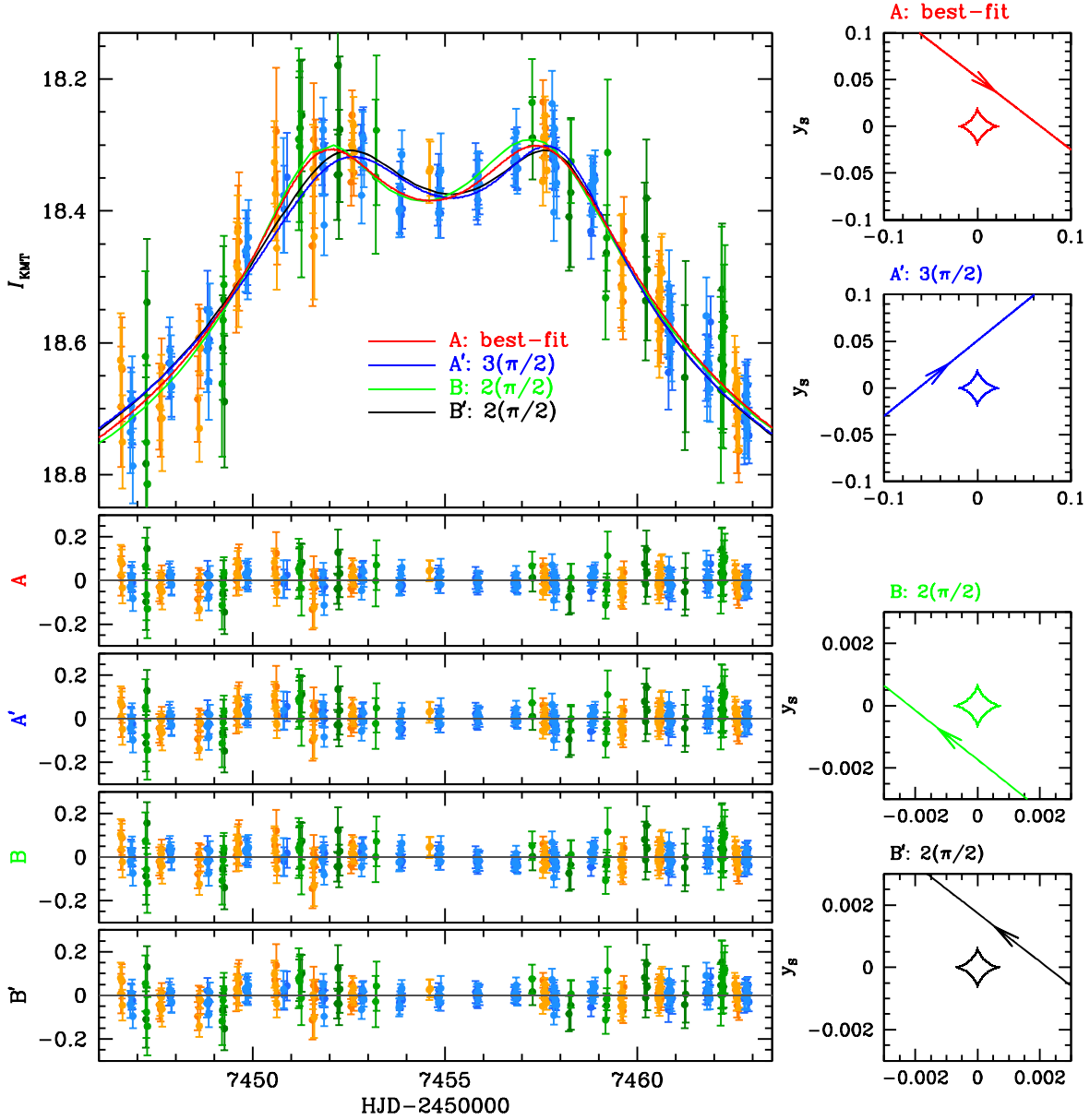
Figure 14. Light curve of KMT-2016-BLG-1855 with the best-fit (A) and degenerate (A′, B, and B′) models.

5.2. OGLE-2016-BLG-1635

For the Bayesian analysis of this event, we apply constraints obtained from t_E (i.e., the Gaussian weight) and ρ_* weight functions on the Galactic prior because the ρ_* measurements are uncertain and the APRX is not measured. Note that we can evaluate the effect of the ρ_* weight on the posterior before conducting the Bayesian analysis. If the lower limit on the relative lens-source proper motion $\mu_{rel,+3\sigma} \equiv \theta_*/(\rho_{*,+3\sigma} t_E) \lesssim 1 \text{ mas yr}^{-1}$, the effect is minor. As expected (see the μ_{rel} column of Table 10), the effects of ρ_* are minor for both solutions.

The Bayesian results indicate that the lens system of this event consists of an M dwarf host star ($M_{host} \sim 0.4\,M_\odot$) and a super-Jupiter-mass planet with a mass of $M_{planet} \sim 11.5\,M_J$, which is close to the limit of planetary objects. The planet orbits the host with a projected separation of $a_\perp \sim 1.31$ or ~ 3.82 au, which is beyond its snow line. The planetary system

is located in the Galactic bulge at a distance of ~ 6.6 kpc from us. Hence, this event is caused by a typical microlensing planetary system, which is a giant planet orbiting an M dwarf host beyond the snow line (Ida & Lin 2005; Kennedy & Kenyon 2008).

5.3. MOA-2016-BLG-532

For this event, the ρ_* values are measured. Thus, we apply t_E and θ_E constraints on the Bayesian analyses. The lens system of this event consists of a late-type M dwarf host star ($M_{host} \sim 0.1\,M_\odot$) and a super-Neptune-mass planet ($M_{planet} \sim 7.2\,M_N$) orbiting with a projected separation of $a_\perp \sim 0.56$ or ~ 1.36 au. The planetary system is located at a distance of $D_L \sim 7.4$ kpc from us. Similar to OGLE-2016-BLG-1635, this event is also caused by a typical microlensing planet.
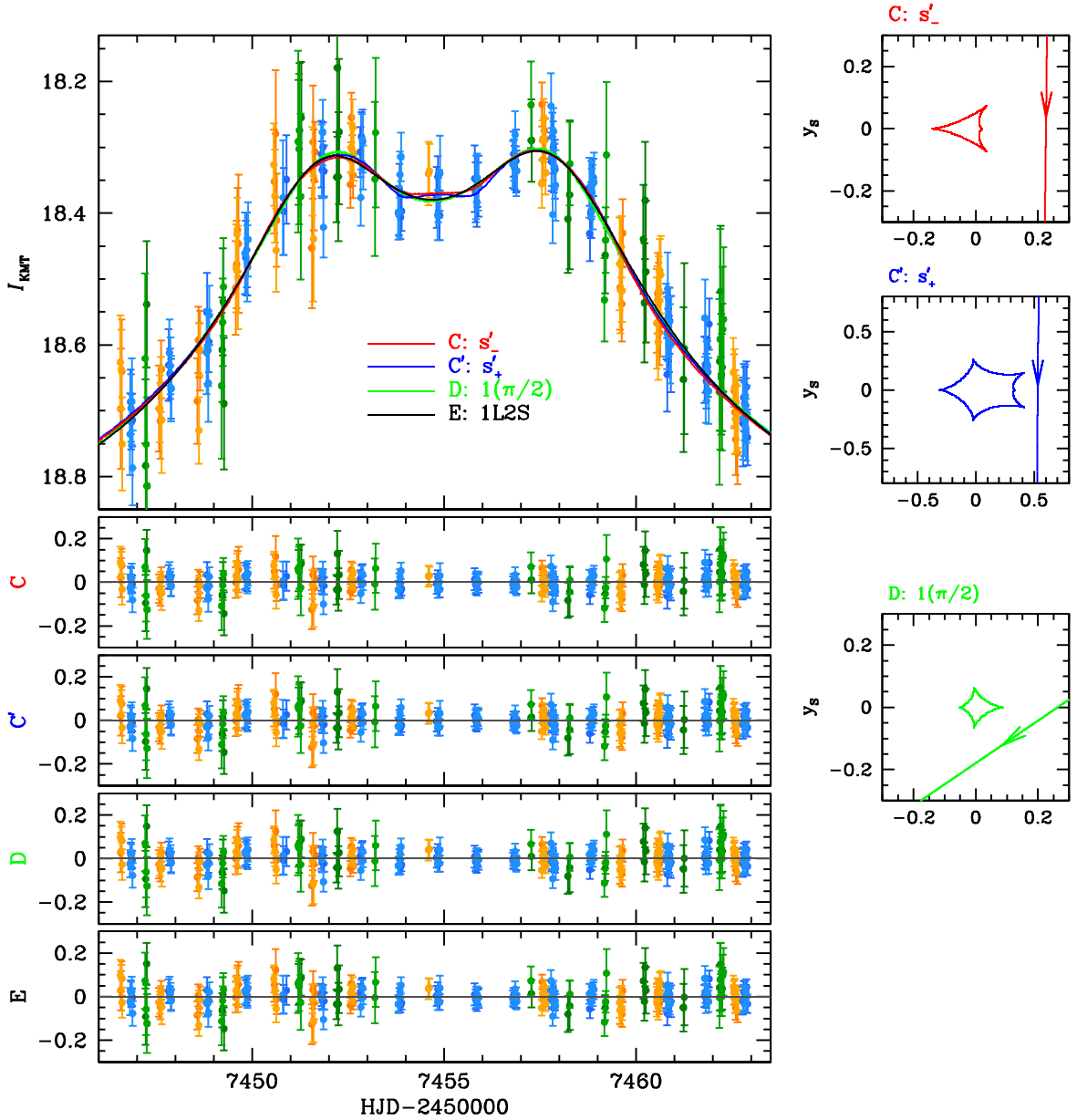
Figure 15. Light curve of KMT-2016-BLG-1855 with degenerate models C, C′, D, and E.

5.4. KMT-2016-BLG-0625

Despite the nonoptimal coverage, we can measure ρ_* for this event. Thus, we apply t_E and θ_E constraints on the Bayesian analyses. For this event, the Bayesian results for the lens system span a wide range of properties because of the degenerate solutions (i.e., due to different q and ρ_* for each solution; see Table 5). The host star is an M dwarf with a mass range of $M_{host} \sim 0.2$–$0.3\,M_{\odot}$. For the s_- case (the best-fit solution), the planet could be a Neptune-mass planet with a mass of $M_{planet} \sim 1.36\,M_N$ orbiting the host with a projected separation of $a_{\perp} \sim 1.3$ au. For the remaining cases, the planet could be a super-Earth-mass planet with a mass range of $M_{planet} \sim 2.0$–$9.0\,M_{\oplus}$ orbiting the host with a projected separation range of $a_{\perp} \sim 0.9$–1.9 au. The planetary system belongs to the Galactic bulge with a distance range of $D_L \sim 6.1$–6.7 kpc.

5.5. OGLE-2016-BLG-1850

For this event, we find the APRX effect on the light curve. However, the ρ_* measurements are uncertain. Thus, we apply t_E, ρ_* weights, and π_E constraints on the Bayesian analyses. The π_E constraints have major effects on the posteriors, while the ρ_* constraints have only minor effects as expected from $\mu_{rel,+3\sigma} \lesssim 1$ mas yr^{-1} (see Table 10).

The planetary system of this event consists of an M dwarf host star ($M_{host} \sim 0.2$–$0.3\,M_{\odot}$) and a super-Earth-mass planet. We find that the planet mass of the inner cases ($M_{planet} \sim 9\,M_{\oplus}$) is smaller than that of the outer cases ($M_{planet} \sim 11\,M_{\oplus}$). The planet orbits the host with a projected separation of $a_{\perp} \sim 1.4$–1.5 au beyond its snow line. The system is located at a distance of $D_L \sim 2$ kpc from us, i.e., in the disk, which is expected by considering the strong microlens parallax effect.
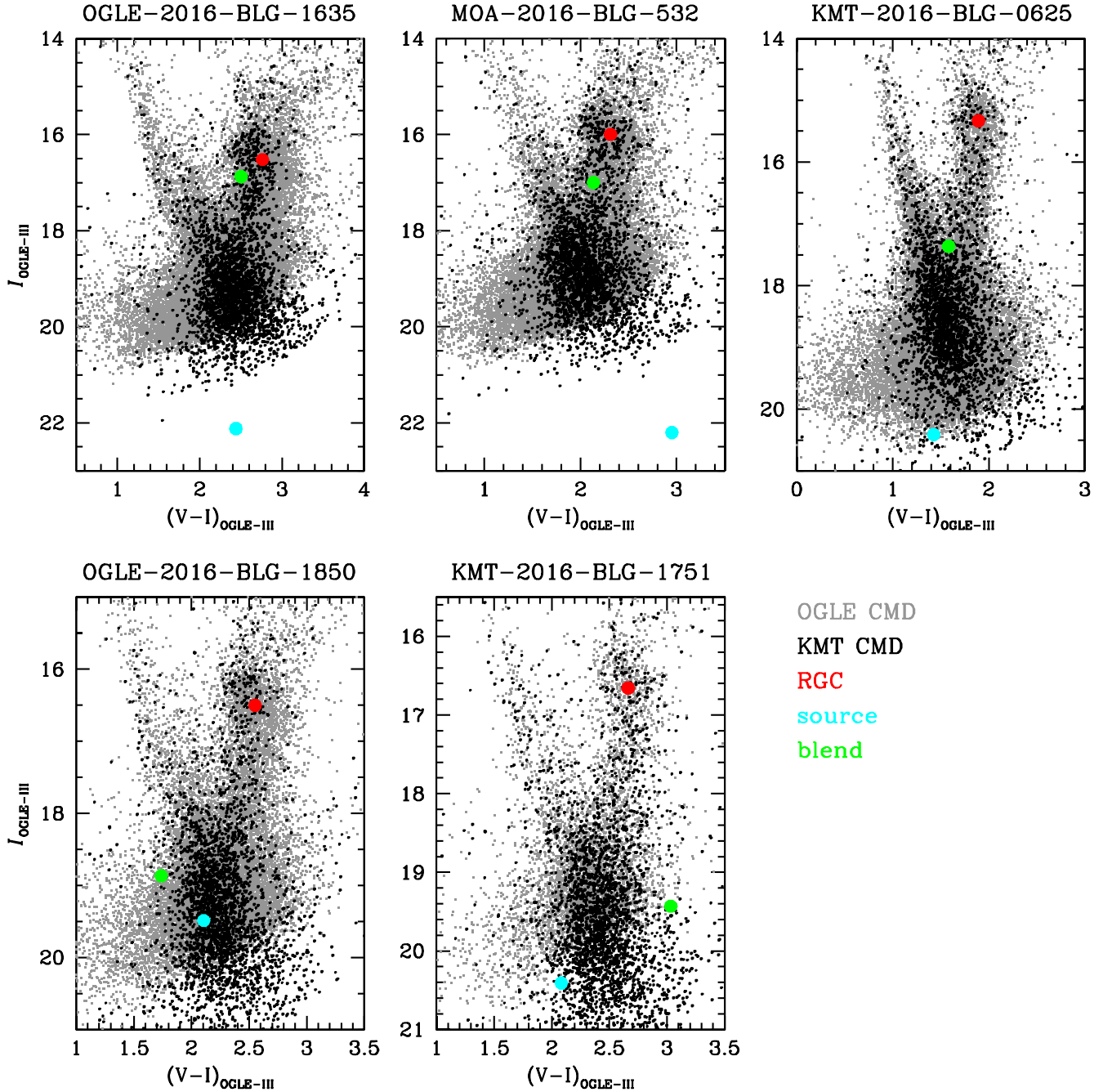
Figure 16. The CMDs of the five planetary events.

5.6. KMT-2016-BLG-1751

For this event, we conduct Bayesian analyses for the $s_\pm$ and $s'_\pm$ solutions by applying t_E and ρ_* weights as constraints. We find that the lens system consists of an M dwarf host ($M_{\rm host} \sim 0.18\,M_\odot$) and a Jupiter-class planet ($M_{\rm planet} \sim 0.7$–$1.2\,M_J$), which is located at a distance of ~ 7.05 kpc from us. The planet orbits the host with a projected separation of $a_\perp \sim 1.2$–1.4 au.

We note that, as mentioned in Section 3.6, the s''_- case is removed from our fiducial solutions. Thus, although we conduct the Bayesian analysis for this case, we do not include its lens properties in Table 11. However, for completeness, we present the lens properties of this case. The Bayesian analysis result using the t_E constraint indicates that the lens system consists of a M dwarf

host star ($M_{\rm host} = 0.18^{+0.28}_{-0.11}\,M_\odot$) and a super-Neptune-mass planet ($M_{\rm planet} = 2.5^{+4.25}_{-1.57}\,M_N$) with a projected separation of $1.28^{+0.54}_{-0.44}$ au. The system is located at a distance of $7.04^{+0.54}_{-1.38}$ kpc, and the relative lens-source proper motion is $\mu_{\rm rel} = 7.56^{+3.45}_{-2.68}$ mas yr^{-1}. The results are similar to the lens properties of our fiducial solutions because the t_E value of s''_- is similar to them, except for the planet mass, which is caused by the smallest q value of the s''_- model. On the other hand, the Bayesian analysis applying t_E and ρ_* weights shows an extreme lens system caused by the unusually small θ_E. That is, the lens system could consist of a very low mass host ($M_{\rm host} = 0.02^{+0.05}_{-0.01}\,M_\odot$) and sub-Neptune-mass planet ($M_{\rm planet} = 0.31^{0.71}_{-0.19}\,M_N$) with a projected separation of $0.31^{+0.06}_{-0.07}$. The system could be located at a distance

Table 10
CMD Analyses of Planetary Events

Event Case	$(V-I)_{\mathrm{RGC}}$ I_{RGC}	$(V-I)_{0,\mathrm{RGC}}$ $I_{0,\mathrm{RGC}}$	$(V-I)_{\mathrm{S}}$ I_{S}	$(V-I)_{0,\mathrm{S}}$ $I_{0,\mathrm{S}}$	$(V-I)_{\mathrm{B}}$ I_{B}	θ_* (μas)	θ_{E} (mas)	μ_{rel} (mas yr^{-1})
OB161635								
s_-	2.763	1.060	2.441 ± 0.136	0.738 ± 0.145	2.503 ± 0.005	0.315 ± 0.050	>0.085	>1.49
	16.519	14.482	22.121 ± 0.015	20.084 ± 0.015	16.872 ± 0.001			
s_+	2.763	1.060	2.442 ± 0.137	0.739 ± 0.145	2.503 ± 0.005	0.311 ± 0.050	>0.076	>1.26
	16.519	14.482	22.153 ± 0.015	20.116 ± 0.015	16.872 ± 0.001			
MB16532								
s_-	2.313	1.060	2.952 ± 0.150	1.699 ± 0.158	2.135 ± 0.002	0.529 ± 0.035	0.113 ± 0.015	1.98 ± 0.26
	15.995	14.391	22.200 ± 0.008	20.596 ± 0.008	16.998 ± 0.001			
s_+	2.313	1.060	2.958 ± 0.150	1.705 ± 0.158	2.135 ± 0.002	0.534 ± 0.036	0.112 ± 0.016	1.99 ± 0.29
	15.995	14.391	22.188 ± 0.008	20.584 ± 0.008	16.997 ± 0.001			
KB160625								
s_-	1.892	1.060	1.427 ± 0.044	0.595 ± 0.066	1.584 ± 0.005	0.364 ± 0.025	0.297 ± 0.029	9.44 ± 0.93
	15.331	14.335	20.412 ± 0.010	19.416 ± 0.010	17.363 ± 0.001			
s_-'	1.892	1.060	1.429 ± 0.044	0.597 ± 0.066	1.583 ± 0.005	0.363 ± 0.025	0.173 ± 0.017	5.46 ± 0.54
	15.331	14.335	20.423 ± 0.010	19.427 ± 0.010	17.362 ± 0.001			
s_+	1.892	1.060	1.429 ± 0.043	0.597 ± 0.066	1.584 ± 0.005	0.368 ± 0.026	0.210 ± 0.021	6.78 ± 0.67
	15.331	14.335	20.390 ± 0.010	19.394 ± 0.010	17.364 ± 0.001			
s_+'	1.892	1.060	1.429 ± 0.043	0.597 ± 0.066	1.584 ± 0.005	0.372 ± 0.026	0.210 ± 0.021	6.85 ± 0.68
	15.331	14.335	20.371 ± 0.010	19.375 ± 0.010	17.366 ± 0.001			
OB161850								
APRX inner $u_0 +$	2.552	1.060	2.106 ± 0.048	0.614 ± 0.069	1.738 ± 0.031	0.880 ± 0.064	>0.126	>0.73
	16.502	14.558	19.488 ± 0.007	17.544 ± 0.007	18.868 ± 0.007			
APRX outer $u_0 +$	2.552	1.060	2.108 ± 0.048	0.616 ± 0.069	1.740 ± 0.030	0.874 ± 0.064	>0.097	>0.56
	16.502	14.558	19.508 ± 0.007	17.564 ± 0.007	18.854 ± 0.006			
APRX inner $u_0 -$	2.552	1.060	2.106 ± 0.048	0.614 ± 0.069	1.743 ± 0.030	0.871 ± 0.064	>0.124	>0.76
	16.502	14.558	19.510 ± 0.007	17.565 ± 0.007	18.848 ± 0.006			
APRX outer $u_0 -$	2.552	1.060	2.108 ± 0.048	0.616 ± 0.069	1.743 ± 0.030	0.873 ± 0.064	>0.097	>0.58
	16.502	14.558	9.511 ± 0.007	17.566 ± 0.007	18.847 ± 0.006			
KB161751								
s_+	2.664	1.060	2.083 ± 0.056	0.479 ± 0.075	3.034 ± 0.068	0.543 ± 0.038	0.039 ± 0.010	>1.06
	16.657	14.548	20.407 ± 0.007	18.299 ± 0.007	19.431 ± 0.004			
s_+'	2.664	1.060	2.083 ± 0.057	0.479 ± 0.076	3.059 ± 0.073	0.554 ± 0.039	0.040 ± 0.011	>1.06
	16.657	14.548	20.366 ± 0.007	18.258 ± 0.007	19.448 ± 0.004			
s_-	2.664	1.060	2.084 ± 0.057	0.480 ± 0.076	2.998 ± 0.062	0.527 ± 0.037	0.041 ± 0.014	>0.94
	16.657	14.548	20.477 ± 0.007	18.368 ± 0.007	19.404 ± 0.004			
s_-'	2.664	1.060	2.084 ± 0.057	0.480 ± 0.076	3.052 ± 0.072	0.551 ± 0.039	0.044 ± 0.015	>1.05
	16.657	14.548	20.375 ± 0.007	18.267 ± 0.007	19.444 ± 0.004			
s_-''	2.664	1.060	2.084 ± 0.057	0.480 ± 0.075	3.047 ± 0.071	0.549 ± 0.039	0.029 ± 0.004	1.09 ± 0.17
	16.657	14.548	20.387 ± 0.007	18.279 ± 0.007	19.439 ± 0.004			

Note. We use abbreviations for event names; e.g., OGLE-2016-BLG-1635 is abbreviated as OB161635.

of $8.17^{+1.05}_{-1.04}$ kpc. The relative lens-source proper motion is $\mu_{\mathrm{rel}} = 1.59^{+0.21}_{-0.34}$ mas yr^{-1}, which is inconsistent with the typical value of the bulge-lens/bulge-source microlensing event (5–10 mas yr^{-1}). If the lens star were resolved by future adaptive optics imaging, this could definitively rule out the s_-'' solution.

6. Summary

We found five new planetary systems and one planet candidate through a systematic anomaly search for the 2016 prime fields of the KMTNet data archive. These "buried" planets have various properties. For OGLE-2016-BLG-1635, the planetary system consists of an M dwarf host ($M_{\mathrm{host}} \sim 0.4\,M_\odot$) and a super-Jupiter-mass planet ($M_{\mathrm{planet}} \sim 11.5\,M_{\mathrm{J}}$) that orbits the host with a projected separation of 1.3 or 3.8 au. The system is located at a

distance of $\sim$6.6 kpc from us. For MOA-2016-BLG-532, the lens system indicates that a super-Neptune-mass planet ($M_{\mathrm{planet}} \sim 7.2\,M_{\mathrm{N}}$) orbits a late M dwarf host star ($M_{\mathrm{host}} \sim 0.1\,M_\odot$) with a projected separation of 0.6 or 1.4 au. The planetary system is located at a distance of $\sim$7.4 kpc from us. For KMT-2016-BLG-0625, because of the degenerate solutions, the planetary system consists of an M dwarf host star with mass in the range 0.1–0.3 $M_\odot$ and a planet with mass in the range 2.0 $M_\oplus$–1.4 M_{N}. The system is located at a distance of 6.1–6.7 kpc. For OGLE-2016-BLG-1850, the planetary system consists of an M dwarf host star ($M_{\mathrm{host}} \sim 0.3\,M_\odot$) and a super-Earth-mass planet ($M_{\mathrm{planet}} = 9$–$11\,M_\oplus$) with a projected separation of $\sim$1.5 au. The system is located at a distance of 2 kpc. For KMT-2016-BLG-1751, we adopt the lens properties of the $s_\pm$ and $s_\pm^\dagger$ cases, which indicate that a Jupiter-class planet ($M_{\mathrm{planet}} = 0.7$–$1.2\,M_{\mathrm{J}}$) orbits an

Table 11
Lens Properties of Planetary Events

Event	Constraints	Case	M_{host} $(M_\odot)$	M_{planet} $(M_J/M_N/M_\oplus)$	D_L (kpc)	$a_\perp$ (au)	μ_{rel} (mas yr^{-1})	Gal. Mod.	χ^2
OB161635	$t_E + \rho_*$	s_-	$0.43^{+0.33}_{-0.27}$	$11.49^{+8.91}_{-7.25}\,M_J$	$6.62^{+1.15}_{-1.68}$	$1.31^{+0.50}_{-0.47}$	$6.32^{+2.89}_{-2.25}$	1.000	1.000
		s_+	$0.44^{+0.33}_{-0.27}$	$11.48^{+8.57}_{-7.28}\,M_J$	$6.60^{+1.15}_{-1.71}$	$3.82^{+1.43}_{-1.37}$	$6.14^{+2.82}_{-2.20}$	0.723	0.021
Adopted			0.43 ± 0.29	$11.49 \pm 7.96\,M_J$	6.62 ± 1.39	1.34 ± 0.47	6.32 ± 2.53		
MB16532	$t_E + \theta_E$	s_-	$0.09^{+0.14}_{-0.05}$	$7.18^{+11.35}_{-3.90}\,M_N$	$7.38^{+0.97}_{-1.02}$	$0.56^{+0.10}_{-0.10}$	$2.10^{+0.30}_{-0.28}$	1.000	0.520
		s_+	$0.09^{+0.15}_{-0.05}$	$7.23^{+11.46}_{-4.05}\,M_N$	$7.37^{+0.97}_{-1.02}$	$1.36^{+0.26}_{-0.25}$	$2.14^{+0.34}_{-0.31}$	0.997	1.000
Adopted			0.09 ± 0.07	$7.21 \pm 5.73\,M_N$	7.37 ± 0.74	1.09 ± 0.17	2.13 ± 0.23		
KB160625	$t_E + \theta_E$	s_-	$0.30^{+0.30}_{-0.16}$	$1.36^{+1.90}_{-0.73}\,M_N$	$6.14^{+0.95}_{-1.28}$	$1.31^{+0.24}_{-0.28}$	$9.25^{+0.98}_{-0.97}$	1.000	1.000
		s_-'	$0.15^{+0.21}_{-0.08}$	$8.98^{+17.84}_{-5.20}\,M_\oplus$	$6.68^{+0.94}_{-1.04}$	$0.86^{+0.15}_{-0.15}$	$5.53^{+0.58}_{-0.57}$	0.365	0.603
		s_+	$0.19^{+0.26}_{-0.10}$	$4.68^{+6.42}_{-2.92}\,M_\oplus$	$6.52^{+0.94}_{-1.11}$	$1.85^{+0.33}_{-0.35}$	$6.80^{+0.72}_{-0.70}$	0.556	0.612
		s_+'	$0.19^{+0.26}_{-0.10}$	$2.03^{+3.53}_{-1.06}\,M_\oplus$	$6.51^{+0.94}_{-1.11}$	$1.84^{+0.33}_{-0.34}$	$6.85^{+0.71}_{-0.69}$	0.574	0.193
Adopted			0.25 ± 0.14	$0.94 \pm 0.80\,M_N$	6.31 ± 0.71	1.40 ± 0.17	8.10 ± 0.61		
OB161850	$t_E + \rho_* + \pi_E$	APRX inner $u_0 +$	$0.26^{+0.20}_{-0.12}$	$8.85^{+7.03}_{-4.19}\,M_\oplus$	$2.12^{+1.17}_{-0.80}$	$1.46^{+0.22}_{-0.26}$	$5.09^{+3.94}_{-2.30}$	0.905	1.000
		APRX outer $u_0 +$	$0.26^{+0.20}_{-0.12}$	$10.73^{+8.59}_{-5.36}\,M_\oplus$	$2.14^{+1.19}_{-0.82}$	$1.49^{+0.22}_{-0.27}$	$4.95^{+3.94}_{-2.28}$	0.914	0.306
		APRX inner $u_0 -$	$0.24^{+0.20}_{-0.11}$	$8.70^{+7.20}_{-3.98}\,M_\oplus$	$2.09^{+1.13}_{-0.79}$	$1.41^{+0.20}_{-0.24}$	$5.17^{+4.09}_{-2.32}$	0.923	0.190
		APRX outer $u_0 -$	$0.26^{+0.20}_{-0.12}$	$11.47^{+9.05}_{-5.70}\,M_\oplus$	$2.22^{+1.19}_{-0.83}$	$1.50^{+0.26}_{-0.28}$	$5.17^{+3.94}_{-2.37}$	1.000	0.070
Adopted			0.26 ± 0.11	$9.33 \pm 3.88\,M_\oplus$	2.12 ± 0.67	1.46 ± 0.16	5.07 ± 2.11		
KB161751	$t_E + \rho_*$	s_+	$0.18^{+0.28}_{-0.11}$	$1.21^{+1.88}_{-0.76}\,M_J$	$7.05^{+1.16}_{-1.38}$	$1.40^{+0.60}_{-0.49}$	$7.49^{+3.46}_{-2.70}$	0.835	1.000
		s_+'	$0.17^{+0.27}_{-0.11}$	$0.73^{+1.14}_{-0.48}\,M_J$	$7.05^{+1.16}_{-1.38}$	$1.36^{+0.58}_{-0.48}$	$7.51^{+3.48}_{-2.71}$	0.719	0.014
		s_-	$0.18^{+0.28}_{-0.12}$	$1.18^{+1.82}_{-0.74}\,M_J$	$7.05^{+1.15}_{-1.38}$	$1.16^{+0.50}_{-0.41}$	$7.37^{+3.42}_{-2.66}$	1.000	0.058
		s_-'	$0.17^{+0.27}_{-0.11}$	$0.69^{+1.08}_{-0.48}\,M_J$	$7.05^{+1.16}_{-1.37}$	$1.15^{+0.49}_{-0.41}$	$7.49^{+3.47}_{-2.70}$	0.696	0.012
Adopted			0.18 ± 0.18	$1.20 \pm 1.21\,M_J$	7.05 ± 1.17	1.39 ± 0.50	7.49 ± 2.83		

Note. For the planet mass, we present the value in Jupiter (M_J), Neptune (M_N), or Earth ($M_\oplus$) masses as appropriate.

Table 12
Planetary Events Discovered on KMTNet Prime Fields in 2016

Event Name	KMT Name	$\log_{10}(q)$	s	Degeneracy	References
OB160007	KB161991	−5.17	2.83		W. Zang et al. (2023, in preparation)
OB161195[a]	KB160372	−4.34	0.99	c/w, ecliptic	Gould et al. (2023)
OB161850	KB161307	−4.00	0.80	i/o, ecliptic	This work
MB16319	KB161816	−2.41	0.82	i/o	Han et al. (2018)
MB16532	KB160506	−2.39	0.65	c/w	This work
KB161836		−2.35	1.30	c/w, ecliptic	Yang et al. (2020)
MB16227	KB160622	−2.03	0.93		Koshimoto et al. (2017)
OB160596	KB161677	−1.93	1.08		Mróz et al. (2017)
KB162605		−1.92	0.94		Ryu et al. (2021)
OB161190	KB160113	−1.84	0.60	Ecliptic	Ryu et al. (2018)
OB161635	KB160269	−1.59	0.59	c/w	This work
KB160625		−3.63	0.74	c/w	This work
OB160613[b]	KB160017	−2.26	1.06	c/w	Han et al. (2017)
KB161751		−2.19	1.05	c/w	This work
KB161855[c]		−1.61	3.80	c/w, α, offset, 1L2S	This work
KB160212		−1.43	0.83	c/w	Hwang et al. (2018)
KB161820		−0.95	1.40		Jung et al. (2018)
KB162142[c]		−0.69	0.97	c/w	Jung et al. (2018)

Notes.
[a] The properties of the planetary system OB161195 were reported by Shvartzvald et al. (2017) and Bond et al. (2017). However, we adopt $\log_{10}(q)$ and s values from Gould et al. (2023), who reanalyzed the event and measured a more precise mass ratio.
[b] For OB160613, the event was caused by a lens system consisting of a planet and binary host stars.
[c] For KB161855 and KB162142, these are planet candidates. In the Degeneracy column, we present the types of degeneracy for the solutions; "c/w," "i/o," "ecliptic," "offset," "α," and "1L2S" indicate the close/wide, inner/outer, ecliptic of the microlens parallax effect, offset, α (see Section 3.7), and 2L1S/1L2S degeneracies, respectively.

M dwarf host ($M_{host} \sim 0.18\,M_\odot$). The system is located at a distance of $\sim$7.05 kpc.

Our goal in the series, including this work, is to build a complete planet sample discovered by the microlensing method for the 2016–2021 KMTNet data archive. As discussed in Zang et al. (2021) and Hwang et al. (2022), such a sample can be used to study the mass-ratio function of microlensing planets. Hence, this work is part of the process of constructing such a sample from the AnomalyFinder candidates. In Table 12, we present all microlensing planets discovered on the KMTNet prime fields in 2016, which are published planets that are recovered by the AnomalyFinder and the five newly discovered in this work. The horizontal line separates the planets expected to be part of the final statistical sample and those whose mass ratios are likely too uncertain or large to be included.

As discussed in Clanton & Gaudi (2014a, 2014b) and Shin et al. (2019), each planet detection method has a different detection sensitivity, which provides complementary planet samples for studying planet demographics and frequency in our Galaxy. Our works are important for a complete microlensing planet sample. Indeed, although the sample size of microlensing planets is relatively small compared to other methods, such as radial velocity and transits, the microlensing planet sample is less biased to host mass because, in principle, the microlensing method can detect any foreground objects regardless of their host brightness. Thus, a complete microlensing planet sample can help us to obtain a better understanding of planet demographics in our Galaxy.

Appendix A
Nonplanetary Events

We report on the analysis of binary lens events that are found by AnomalyFinder as candidate planetary events. From the initial analyses, we find that the light curves of these events could be describing both binary and planet lens interpretations. However, based on analyses using TLC reductions, we find that these events disfavor planetary solutions ($q < 0.03$) by $\Delta\chi^2 > 10$. Thus, we cannot claim certain detection of the planets. In Table 2, we present observational information on these events.

A.1. OGLE-2016-BLG-0987

The light curve of OGLE-2016-BLG-0987 (which we identified as KMT-2016-BLG-0020) shows deviations from the 1L1S interpretation ($\Delta\chi^2_{1L1S-2L1S} = 159.68$). From the 2L1S modeling, we find several 2L1S solutions that can explain the deviations. Among the solutions, four are binary lens cases, and three are planet lens cases. The best-fit solution is the binary lens case with $(s,\ q) = (0.492 \pm 0.013,\ 0.108 \pm 0.005)$. However, the lowest χ^2 planetary solution $((s,\ q(\times 10^{-4}) = (0.702 \pm 0.081,\ 59.198 \pm 49.265))$ shows $\Delta\chi^2 = 26.60$ compared to the best-fit solution. The $\Delta\chi^2$ cannot satisfy our criterion to claim the planet detection. Also, the planetary solutions cannot describe the subtle bump feature at $HJD' \sim 7,528$. Thus, we conclude that OGLE-2016-BLG-0987 should be removed from the planet sample. We note that, although this event is not likely to be caused by a planetary lens system, the best-fit solution indicates that the companion could be a low-mass object such as a brown dwarf.

A.2. MOA-2016-BLG-123

For this event (which we identified as KMT-2016-BLG-0106), we find seven local solutions based on analysis using the TLC reductions. However, not all local minima satisfy our q criterion (i.e., $q < 0.03$) for claiming a planet detection. The best-fit solution indicates that the event was caused by a binary lens system, i.e., $(s,\ q) = (2.671 \pm 0.089,\ 1.113 \pm 0.099)$. Among the local minima, the model showing the lowest q value ($q = 0.052 \pm 0.003$) is disfavored by $\Delta\chi^2 = 122.70$ compared to the best-fit solution. Thus, we conclude that this event should be removed from the planet sample.

A.3. OGLE-2016-BLG-0558

For this event (which we identified as KMT-2016-BLG-0157), we found two solutions that showed a planet-like mass ratio ($q \sim 0.03$) from the initial analysis. We therefore refine the solutions based on the TLC reductions. The analysis using the TLC reductions clearly shows localized solutions (i.e., $s_\pm$ cases) with $(s,\ q) = (0.580 \pm 0.009,\ 0.048 \pm 0.003)$ and $(2.158 \pm 0.027,\ 0.057 \pm 0.003)$ for the s_- and s_+ cases, respectively. However, the mass ratios do not satisfy our criterion ($q < 0.03$) to claim the planet detection, although the companion is likely to be a low-mass object such as a brown dwarf. Hence, we remove this event from the planet sample.

A.4. KMT-2016-BLG-0374

We find plausible solutions within the planetary regime ($q < 0.03$) from the initial analysis. However, based on the analysis using TLC reductions, we find that the best-fit solutions are binary lens cases with $(s,\ q) = (6.89,\ 0.55)$ and $(0.20,\ 0.22)$ for the s_+ and s_- cases, respectively. We also find that the planet-like models are disfavored by $\Delta\chi^2 = 19.74$ and 18.60 for the s_+ and s_- cases, respectively. The planet-like solutions cannot satisfy the criterion for the planet detection. Thus, we remove this event from our planet samples.

A.5. KMT-2016-BLG-0446

The AnomalyFinder detects a subtle deviation of the light curve at $HJD' \sim 7,631.0$–$7,636.0$ based on the pipeline data. The anomaly can be explained by planetary models. However, the TLC reductions reveal that the anomaly is a false positive.

Then, we find that the light curve can be explained by the 1L1S interpretation rather than any 2L1S interpretations. Thus, we remove KMT-2016-BLG-0446 from our sample.

A.6. OGLE-2016-BLG-1722

We find that the best-fit solution of OGLE-2016-BLG-1722 (which we identified as KMT-2016-BLG-1716) is caused by a binary lens with the mass ratio $q = 1.247 \pm 0.204$ (i.e., $q \sim 0.80$) for the s_- case (the competing s_+ solution also exists). The best-fit light curves are caused by approaching a diamond-shaped caustic. Thus, a fourfold degeneracy exists (i.e., four solutions with different source trajectories for different α values).

We also find alternative planetary solutions with the mass ratio $q = (26.095 \pm 8.013) \times 10^{-4}$ for the s_- case. However, $\Delta\chi^2_{\mathrm{(planet-binary)}} = 29.23$. The $\Delta\chi^2$ cannot satisfy our criterion ($\Delta\chi^2 < 10$) to claim a planet detection. Indeed, these planetary models clearly show worse fits in their residuals. Hence, we decide to remove OGLE-2016-BLG-1722 from our planet candidate sample for full analysis.

A.7. OGLE-2016-BLG-0974

The best-fit solution of OGLE-2016-BLG-0974 (which we identified as KMT-2016-BLG-1863) is a binary lens model with $(s, q) = (0.277 \pm 0.005, 0.306 \pm 0.031)$. There is an s_+ solution, $(s, q) = (5.626 \pm 0.215, 0.782 \pm 0.133)$, with $\Delta\chi^2 = 6.96$ caused by the close/wide degeneracy. We find that the solutions having the lowest χ^2 in the planetary regime ($q < 0.03$) are disfavored by $\Delta\chi^2 = 78.89$ and 73.52 for the s_-: $[s, q] = [0.576 \pm 0.007, (161.679 \pm 8.552) \times 10^{-4}]$ and s_+: $[s, q] = [1.657 \pm 0.025, (176.374 \pm 10.013) \times 10^{-4}]$ cases, respectively. Thus, we conclude that OGLE-2016-BLG-0974 is caused by a binary rather than a planetary lens system.

Appendix B
OGLE-2016-BLG-0185

We also present the analysis of OGLE-2016-BLG-0185, which was identified by eye as a planet candidate but not selected as anomalous in the AnomalyFinder process. We conduct a detailed analysis based on TLC reductions for this event. We find that the best-fit solution is a binary lens case
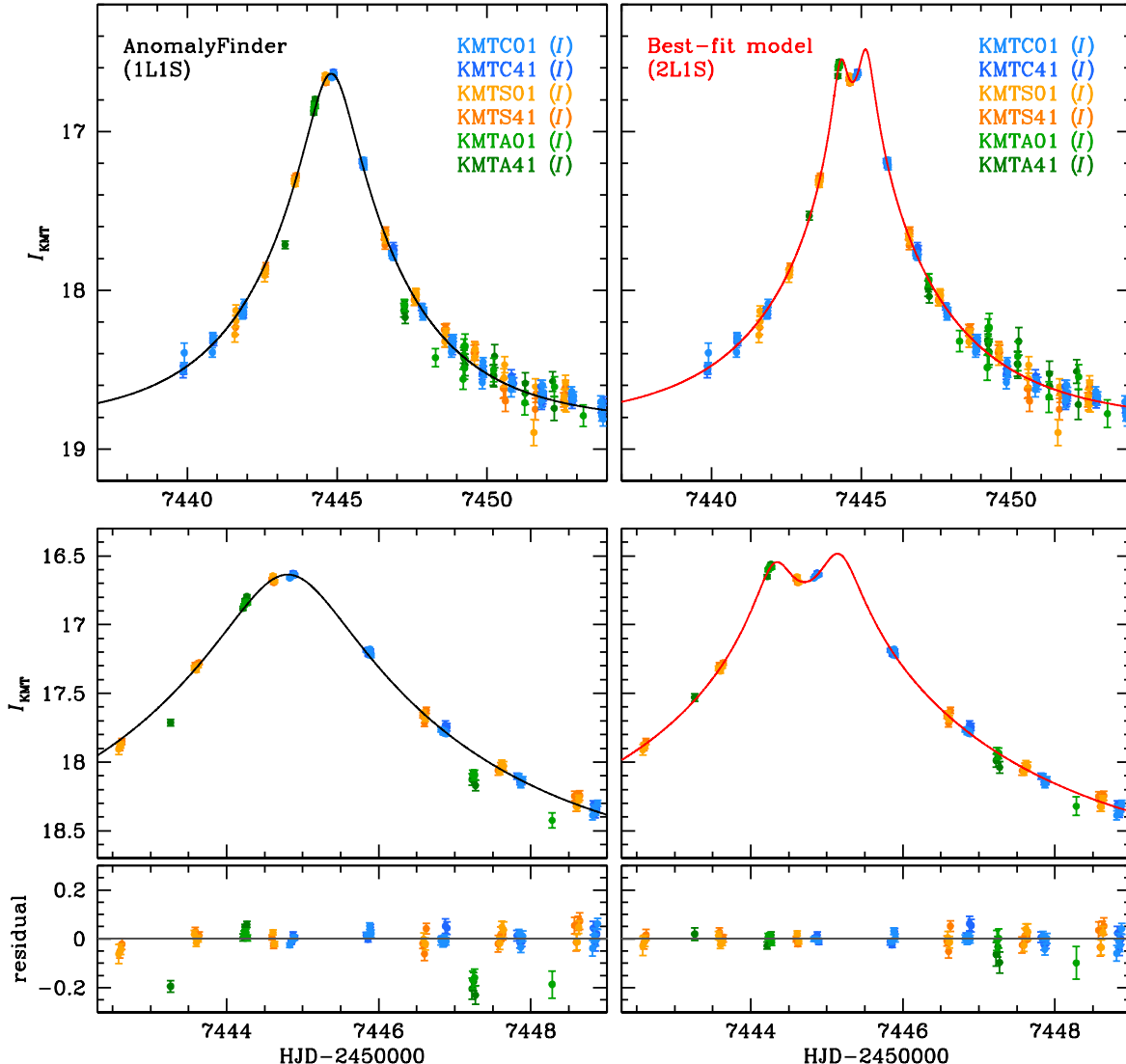

Figure 17. Comparison of light curves between AnomalyFinder (1L1S) and the best fit (2L1S) for OGLE-2016-BLG-0185. Note that the data sets shown in this figure are produced by the KMTNet pipeline, which is actually used for the AnomalyFinder process.

with $(s, q) = (4.834 \pm 0.201, 3.480 \pm 1.110)$. This is equivalent to $\frac{1}{q} = 0.287 \pm 0.085$, which clearly implies a binary lens origin. We also search for a planetary model. The best planetary model that satisfies our mass-ratio criterion has $(s, q) = (0.724 \pm 0.037, 0.013 \pm 0.004)$ but is disfavored by $\Delta\chi^2 = 46$ compared to the best-fit model. Thus, we conclude that this event was caused by a binary lens system.

Although OGLE-2016-BLG-0185 turned out to be a binary lens event, it is still an important test case for verifying the AnomalyFinder process and assessing possible failure modes. In fact, the AnomalyFinder algorithm did identify a series of possible anomalies in this event, but the human operator rejected them as "fake." In OGLE-2016-BLG-0185, the anomaly occurs over the peak of the event, but because the event occurs early in the microlensing season, it is only sparsely covered, and the primary deviation from a point lens only occurs in the KMTA data sets. In addition, the event has a short timescale. Hence, due to the χ^2 likelihood estimation, a point lens fit is biased toward the points at the peak (which have the smallest error bars) and the baseline points (which dominate the numbers), so it normalized the flux levels of the KMTA data so that the peak points (due to the anomaly) lay on the point lens light curve. As a result, the "anomalies" identified by the AnomalyFinder were in the rising and falling parts of the light curve and caused by the bad flux normalization rather than the actual anomaly (see Figure 17).

OGLE-2016-BLG-0185 is qualitatively similar to KMT-2021-BLG-2294, which was also missed by the Anomaly-Finder process (Shin et al. 2023). They are both short-timescale events ($t_{\rm E} = 10.8 \pm 1.3$ and 7.1 ± 0.3 days, respectively) and had anomalies that occurred at the peak of the events. On the other hand, the reasons the anomalies were missed are distinctly different: in OGLE-2016-BLG-0185, the wrong anomaly was identified, but in KMT-2021-BLG-2294, the anomaly did not meet the detection threshold. The latter case is acceptable from the perspective of constructing a statistical sample of events. However, the failure for OGLE-2016-BLG-0185 is more concerning but could be compensated for by adding an additional criterion to the AnomalyFinder algorithm to check for outliers in flux normalization.

ORCID iDs

In-Gu Shin ⦿ https://orcid.org/0000-0002-4355-9838
Jennifer C. Yee ⦿ https://orcid.org/0000-0001-9481-7123
Weicheng Zang ⦿ https://orcid.org/0000-0001-6000-3463
Hongjing Yang ⦿ https://orcid.org/0000-0003-0626-8465
Kyu-Ha Hwang ⦿ https://orcid.org/0000-0002-9241-4117
Cheongho Han ⦿ https://orcid.org/0000-0002-2641-9964
Andrzej Udalski ⦿ https://orcid.org/0000-0001-5207-5619
Michael D. Albrow ⦿ https://orcid.org/0000-0003-3316-4012
Sun-Ju Chung ⦿ https://orcid.org/0000-0001-6285-4528
Yoon-Hyun Ryu ⦿ https://orcid.org/0000-0001-9823-2907
Yossi Shvartzvald ⦿ https://orcid.org/0000-0003-1525-5041
Seung-Lee Kim ⦿ https://orcid.org/0000-0003-0562-5643
Chung-Uk Lee ⦿ https://orcid.org/0000-0003-0043-3925
Byeong-Gon Park ⦿ https://orcid.org/0000-0002-6982-7722
Richard W. Pogge ⦿ https://orcid.org/0000-0003-1435-3053
Michał K. Szymański ⦿ https://orcid.org/0000-0002-0548-8995
Jan Skowron ⦿ https://orcid.org/0000-0002-2335-1730
Radosław Poleski ⦿ https://orcid.org/0000-0002-9245-6368
Igor Soszyński ⦿ https://orcid.org/0000-0002-7777-0842

Paweł Pietrukowicz ⦿ https://orcid.org/0000-0002-2339-5899
Szymon Kozłowski ⦿ https://orcid.org/0000-0003-4084-880X
Patryk Iwanek ⦿ https://orcid.org/0000-0002-6212-7221
Krzysztof Ulaczyk ⦿ https://orcid.org/0000-0001-6364-408X
Marcin Wrona ⦿ https://orcid.org/0000-0002-3051-274X
Mariusz Gromadzki ⦿ https://orcid.org/0000-0002-1650-1518
Richard Barry ⦿ https://orcid.org/0000-0003-4916-0892
David P. Bennett ⦿ https://orcid.org/0000-0001-8043-8413
Akihiko Fukui ⦿ https://orcid.org/0000-0002-4909-5763
Yuki Hirao ⦿ https://orcid.org/0000-0003-4776-8618
Yoshitaka Itow ⦿ https://orcid.org/0000-0002-8198-1968
Iona Kondo ⦿ https://orcid.org/0000-0002-3401-1029
Naoki Koshimoto ⦿ https://orcid.org/0000-0003-2302-9562
Yutaka Matsubara ⦿ https://orcid.org/0000-0002-9629-4810
Shota Miyazaki ⦿ https://orcid.org/0000-0001-9818-1513
Yasushi Muraki ⦿ https://orcid.org/0000-0003-1978-2092
Greg Olmschenk ⦿ https://orcid.org/0000-0001-8472-2219
Clément Ranc ⦿ https://orcid.org/0000-0003-2388-4534
Nicholas J. Rattenbury ⦿ https://orcid.org/0000-0001-5069-319X
Yuki Satoh ⦿ https://orcid.org/0000-0002-1228-4122
Takahiro Sumi ⦿ https://orcid.org/0000-0002-4035-5012
Daisuke Suzuki ⦿ https://orcid.org/0000-0002-5843-9433

References

Alard, C., & Lupton, R. H. 1998, ApJ, 503, 325
Albrow, M. D. 2017, MichaelDAlbrow/pyDIA: Initial Release on github, V1.0.0, Zenodo, doi:10.5281/zenodo.268049
Albrow, M. D., Horne, K., Bramich, D. M., et al. 2009, MNRAS, 397, 2099
Bensby, T., Adén, D., Meléndez, J., et al. 2011, A&A, 533, A134
Bond, I. A., Abe, F., Dodd, R. J., et al. 2001, MNRAS, 327, 868
Bond, I. A., Bennett, D. P., Sumi, T., et al. 2017, MNRAS, 469, 2434
Bramich, D. M., Horne, K., Albrow, M. D., et al. 2013, MNRAS, 428, 2275
Chang, K., & Refsdal, S. 1979, Natur, 282, 561
Clanton, C., & Gaudi, B. S. 2014a, ApJ, 791, 90
Clanton, C., & Gaudi, B. S. 2014b, ApJ, 791, 91
Doran, M., & Müller, C. M. 2004, JCAP, 2004, 003
Gaudi, B. S. 1998, ApJ, 506, 533
Gaudi, B. S., & Gould, A. 1997, ApJ, 486, 85
Gonzalez, O. A., Rejkuba, M., Zoccali, M., et al. 2012, A&A, 543, A13
Gould, A. 1992, ApJ, 392, 442
Gould, A. 2022, arXiv:2209.12501
Gould, A., Han, C., Zang, W., et al. 2022, A&A, 664, A13
Gould, A., & Loeb, A. 1992, ApJ, 396, 104
Gould, A., Shvartzvald, Y., Zhang, J., et al. 2023, arXiv:2303.08876
Griest, K., & Hu, W. 1992, ApJ, 397, 362
Griest, K., & Safizadeh, N. 1998, ApJ, 500, 37
Han, C., Bond, I. A., Gould, A., et al. 2018, AJ, 156, 226
Han, C., & Gould, A. 1997, ApJ, 480, 196
Han, C., Udalski, A., Gould, A., et al. 2017, AJ, 154, 223
Hwang, K.-H., Kim, H.-W., Kim, D.-J., et al. 2018, JKAS, 51, 197
Hwang, K.-H., Zang, W., Gould, A., et al. 2022, AJ, 163, 43
Ida, S., & Lin, D. N. C. 2005, ApJ, 626, 1045
Jung, Y. K., Hwang, K.-H., Ryu, Y.-H., et al. 2018, AJ, 156, 208
Jung, Y. K., Zang, W., Han, C., et al. 2022, AJ, 164, 262
Jung, Y. K., Zang, W., Wang, H., et al. 2023, AJ, 165, 226
Kennedy, G. M., & Kenyon, S. J. 2008, ApJ, 673, 502
Kervella, P., Thévenin, F., Di Folco, E., et al. 2004, A&A, 426, 297
Kim, D.-J., Kim, H.-W., Hwang, K.-H., et al. 2018, AJ, 155, 76
Kim, S.-L., Lee, C.-U., Park, B.-G., et al. 2016, JKAS, 49, 37
Koshimoto, N., Shvartzvald, Y., Bennett, D. P., et al. 2017, AJ, 154, 3
Minniti, D., Lucas, P., & Team, V. V. V. 2017, VizieR Online Data Catalog, II/348
Mróz, P., Han, C., Udalski, A., et al. 2017, AJ, 153, 143
Nataf, D. M., Gould, A., Fouqué, P., et al. 2013, ApJ, 769, 88
Paczynski, B. 1997, arXiv:astro-ph/9711007
Pecaut, M. J., & Mamajek, E. E. 2013, ApJS, 208, 9
Pecaut, M. J., Mamajek, E. E., & Bubar, E. J. 2012, ApJ, 746, 154

Poindexter, S., Afonso, C., Bennett, D. P., et al. 2005, ApJ, 633, 914
Ryu, Y.-H., Hwang, K.-H., Gould, A., et al. 2019, AJ, 158, 151
Ryu, Y.-H., Hwang, K.-H., Gould, A., et al. 2021, AJ, 162, 96
Ryu, Y.-H., Kil Jung, Y., Yang, H., et al. 2022, AJ, 164, 180
Ryu, Y.-H., Yee, J. C., Udalski, A., et al. 2018, AJ, 155, 40
Shin, I.-G., Ryu, Y.-H., Yee, J. C., et al. 2019, AJ, 157, 146
Shin, I.-G., Yee, J. C., Gould, A., et al. 2023, AJ, 165, 8
Shvartzvald, Y., Yee, J. C., Calchi Novati, S., et al. 2017, ApJL, 840, L3
Sumi, T., Abe, F., Bond, I. A., et al. 2003, ApJ, 591, 204
Szymański, M. K., Udalski, A., Soszyński, I., et al. 2011, AcA, 61, 83
Tomaney, A. B., & Crotts, A. P. S. 1996, AJ, 112, 2872
Udalski, A. 2003, AcA, 53, 291

Udalski, A., Szymanski, M., Kaluzny, J., et al. 1994, AcA, 44, 227
Udalski, A., Szymański, M. K., & Szymański, G. 2015, AcA, 65, 1
Wang, H., Zang, W., Zhu, W., et al. 2022, MNRAS, 510, 1778
Wozniak, P. R. 2000, AcA, 50, 421
Yang, H., Zhang, X., Hwang, K.-H., et al. 2020, AJ, 159, 98
Yee, J. C., Shvartzvald, Y., Gal-Yam, A., et al. 2012, ApJ, 755, 102
Yoo, J., DePoy, D. L., Gal-Yam, A., et al. 2004, ApJ, 603, 139
Zang, W., Hwang, K.-H., Udalski, A., et al. 2021, AJ, 162, 163
Zang, W., Jung, Y. K., Yang, H., et al. 2023, AJ, 165, 103
Zang, W., Yang, H., Han, C., et al. 2022a, MNRAS, 515, 928
Zhang, K., & Gaudi, B. S. 2022, ApJL, 936, L22
Zhang, K., Gaudi, B. S., & Bloom, J. S. 2022b, NatAs, 6, 782